Geophys. J. Int. (2005) **160,** 227–248 doi: 10.1111/j.1365-246X.2004.02470.x

Crustal structure and earthquake focal depths beneath northeastern India and southern Tibet

Supriyo Mitra,[1] Keith Priestley,[1] Anjan Kr Bhattacharyya[2] and V. K. Gaur[3,4]

[1] *Bullard Laboratories, University of Cambridge, UK*
[2] *Department of Mathematics, Tezpur University, Assam, India*
[3] *Indian Institute of Astrophysics, Bangalore, India*
[4] *Center for Mathematical Modelling and Computer Simulations, Bangalore, India*

Accepted 2004 September 3. Received 2004 September 2; in original form 2003 August 21

SUMMARY

We use broad-band teleseismic data recorded at eight sites along a north–south profile from Karimganj (24.84°N, 92.34°E), south of the eastern Shillong Plateau, to Bomdilla (27.27°N, 92.41°E) in the eastern Lesser Himalaya, to determine the seismic characteristics of the crust in northeastern India. We also analyse data from the Chinese Digital Seismic Network station at Lhasa and INDEPTHII stations located on the southern Tibetan Plateau north of our profile, to extend the seismic images of the crust further northwards. Although the northeastern Indian stations and the Tibetan stations do not lie along a linear profile across the Himalaya, the well-recognized uniformity of the Himalaya along strike make this comparison of the two profiles meaningful. Receiver functions calculated from these data show that the crust is thinnest (∼35–38 km) beneath the Shillong Plateau. Receiver functions at Cherrapunji, on the southern edge of the Shillong Plateau, have a strong azimuthal dependence. Those from northern backazimuth events show that the Moho beneath the southernmost Shillong Plateau is at a depth of ∼38 km while receiver functions from southern backazimuth events indicate that the Moho beneath the northernmost Bengal Basin is at a depth of ∼44 km. Receiver functions from sites on the Brahmaputra Valley demonstrate that the Moho is deeper by ∼5–7 km than below the Shillong Plateau, a result which agrees with the hypothesis that the Shillong Plateau is supported by shearing stress on two steep faults that cut through the crust. Further north of the eastern Himalayan foredeep, the Moho dips gently northwards, reaching a depth of ∼48 km beneath Bomdilla in the Lesser Himalaya, and 88 km below Lhasa in Tibet. Using the crustal velocity models obtained from receiver function inversions, we redetermined focal depths of well-recorded earthquakes across this part of the Indo-Tibetan collision zone and find all of these to occur within the crust. Hence we find no evidence for bimodal depth distribution of earthquakes beneath this region of northeastern India.

Key words: crustal structure, earthquake depths, Eastern Himalaya, India, Shillong Plateau, Tibetan Plateau.

1 INTRODUCTION

It is generally thought that the simultaneous underthrusting of northeast India beneath the nearly perpendicular Himalayan and Burmese arcs (Fig. 1) is responsible for the high, diffused seismicity of the region. However, several important questions remain unanswered, notably the uncompensated altitude of the Shillong Plateau, the Moho geometry of the Indian crust as it underthrusts the Himalaya and southern Tibet, and whether there is a bimodal depth distribution of seismicity beneath this region. This paper presents results of an experiment designed to address these issues. We first discuss the seismic characteristics of the crust determined from receiver function analysis of data recorded along a ∼550 km long north–south profile (Fig. 1) extending from Karimganj (24.84°N, 92.34°E) in the northernmost Bengal Basin through the Shillong Plateau, the Eastern Himalaya to Lhasa (29.7°N, 91.15°E) on the Tibetan Plateau. We then use this new information on the crustal structure to redetermine earthquake focal depths across the Indo-Tibetan collision zone in northeast India.

The most spectacular tectonic feature of the region is the Eastern Himalaya, a stack of east–west striking thrust sheets composed of crystalline rocks of the great Himalaya and the metasedimentary Lesser Himalaya separated by the Pan-Himalayan Main Central Thrust (MCT). These thrust sheets have advanced over the Indian Shield as a result of India's underthrusting of Tibet (e.g. Gansser 1964; Le Fort 1975), a process which continues at present by slip on

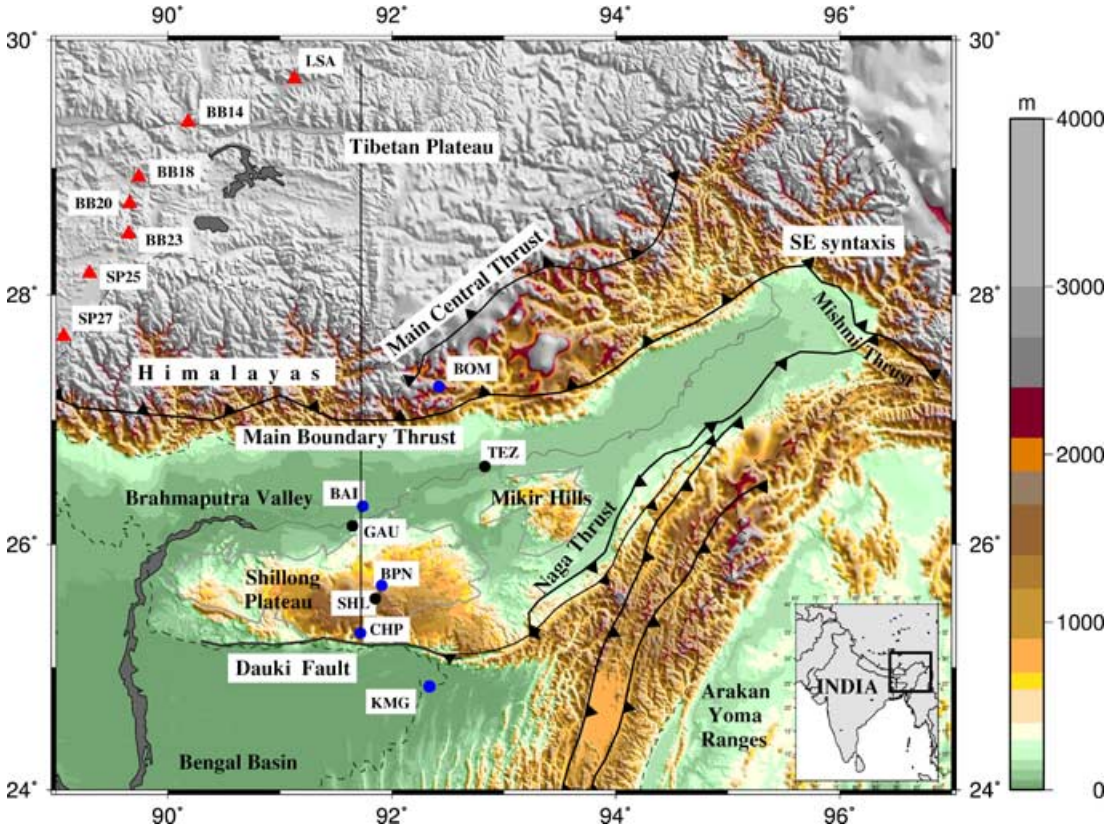

Figure 1. Topographic map of northeast India (boxed area on the inset map of India), showing the main tectonic units of the region and the location of seismic stations (black circles, Cambridge University (CU) and Indian Institute of Astrophysics (IIA) BB stations; grey triangles, NGRI (TEZ), IMD (SHL) and Gauhati University (GAU) BB stations; white triangles, INDEPTHII and CDSN stations) which recorded data for this study.

the décollement surface, the splays of which constitute the southern Himalayan thrust front. Of these, the Main Boundary Thrust (MBT) has been geologically mapped all along the Himalaya, and its present activity is testified by both well-constrained earthquake focal mechanisms (Baranowski *et al.* 1984; Ni & Barazangi 1984; Molnar & Pandey 1989; Holt *et al.* 1991) and GPS Geodesy (Bilham *et al.* 1997).

The second prominent structural feature of northeast India is the elevated block of Archean–Proterozoic basement exposed in the Shillong Plateau and Mikir Hills. The Shillong Plateau, which rises to ∼1 km above the Bangladesh plains, is bound on the south by the steep north-dipping (Bilham & England 2001) Dauki Fault, a geomorphic feature of precipitous relief. The Dauki Fault together with its east-northeastward extension the Disang Fault, marks the northern limit of the Cretaceous age (∼120 Ma) Sylhet flood basalts that were extruded across the region during the break-up of India from Antarctica, suggesting that the fault pre-dates the basalt flows. Using seismic depth estimates to the top of the Sylhet limestone in the trough south of the Dauki Fault and comparing them with exposures north of the fault, Hiller (1988) estimated that the Shillong Plateau has been uplifted by ∼15 km along the Dauki Fault. Bilham & England (2001) infer the existence of a high-angled reverse fault (the Oldham Fault) along the northern edge of the plateau, which ruptured during the 1897 earthquake, uplifting the plateau by 11 m. This fault, although unmapped at the surface, most likely post-dates the Dauki Fault and was formed after the India–Eurasian collision when the region entered the compressional regime. Thereafter, movement on the two faults has uplifted the Shillong Plateau.

Other significant geological features of the region are the Brahmaputra Valley and the Bengal Basin north and south, respectively, of the Shillong Plateau. The basement in the lower Brahmaputra Valley is exposed in low-lying ridges on either side of the river, where it underlies only ∼100 m of recent alluvium. Further north, beneath the Himalayan foredeep, the basement is covered by gently dipping Tertiary sediments and recent alluvium that increase in thickness to 4–5 km along the northern Himalayan front and a little less along the northeastern Himalayan front. Nandy & Das Gupta (1986) used satellite images to identify a number of buried lineaments beneath the alluvium in the Brahmaputra Valley. Prominent among these are the east–west striking Brahmaputra Fault along the northern edge of the Shillong Plateau, almost paralleling the river, and the northwest–southeast trending Kopili River lineament between the Shillong Plateau and the Mikir Hills. The Bengal Basin, which includes the world's largest delta, is mostly covered by recent alluvium underlain by a complete sequence of Tertiary sediments, thickening eastwards to ∼20 km. Geophysical surveys and deep drilling in the region have enabled a more detailed characterization of its sedimentary section (Das Gupta & Biswas 2000; Shamsuddin & Abdullah 1997). To the east, the Indo-Burman fold and thrust belt actively overthrusts the Indian continental basement and its Palaeogene–Neogene cover along a stack of imbricate thrusts and have resulted in both shallow and moderate-depth earthquakes in the region (Chen & Molnar 1990; Hallet & Molnar 2001).

Table 1. Station name, location, backazimuth and delta bins and number of receiver functions stacked, average crustal V_s and crustal thickness obtained from the inversion of receiver functions for the stations used in this study. CHP is given twice for the events from the northeast (CHP-N) and southeast (CHP-S).

Station	Lat. (°N)	Long. (°E)	BAZ (°)	Δ(°)	No. of RFs	V_s (km s^{-1})	Moho depth (km)
KMG	24.8466	92.3435	38–42	60–68	2	3.53	39
CHP-S	25.2806	91.7235	106–125	45–66	9	3.63	44
CHP-N	25.2806	91.7235	52–86	36–48	6	3.76	38
SHL	25.5663	91.8558	86–109	51–65	3	3.77	35
BPN	25.6698	91.9088	52–72	44–48	3	3.76	35
GAU	26.1500	91.6500	302	21	2	3.63	40
BAI	26.3183	91.7399	107–117	67–76	10	3.86	42
TEZ	26.6333	92.8333	89–130	37–57	7	3.83	42
BMD	27.2713	92.4181	90–119	51–61	10	3.58	48
SP27	27.6712	89.0762	50–55	48–54	12	3.62	62
SP25	28.1778	89.3029	50–55	47–53	15	3.72	68
BB23	28.4856	89.6585	44–55	47–54	6	3.63	62
BB20	28.7273	89.6643	145–146	39–45	5	3.65	76
BB18	28.9301	89.7440	145–146	39–45	4	3.61	76
BB14	29.3682	90.1845	44–57	46–54	12	3.65	80
LSA	29.7000	91.1499	42–129	40–55	30	3.74	88

2 DATA AND METHODOLOGY

Since mid-2001 we have operated five broad-band seismographs in northeast India (Fig. 1). Each station consists of a Guralp CMG3TDM sensor with a flat velocity response between 0.0083 and 50 Hz, and a Guralp SAM data logger. Data were continuously recorded at 100 samples per second and time-stamped using a GPS receiver. In this study, we analyse data from these five stations plus three broad-band stations operated by other institutions. The seismograph at Karimgunj (KMG) is located on the sediments of the Bengal Basin south of the Shillong Plateau; Cherrapunji (CHP), Shillong (SHL) and Barapani (BPN) lie on the Precambrian crystalline basement exposures on the Shillong Plateau; Bahiata (BAI), Gauhati (GAU) and Tezpur (TEZ) are on the low-lying basement ridges in the Brahmaputra Valley, and Bomdilla (BMD) is located on bedrock in the Lesser Himalaya north of the MBT and a few kilometres south of the MCT (Fig. 1). TEZ is operated by the National Geophysical Research Institute (NGRI), SHL by the Indian Meteorological Department (IMD) and GAU by Gauhati University. In addition to data from these Indian stations, we reanalyse data from six INDEPTHII stations (SP27, SP25, BB23, BB20, BB18 and BB14: Fig. 1) and the permanent Chinese Digital Seismic Network (CDSN) station at Lhasa (LSA: Fig. 1), all located on the Tibetan Plateau. TEZ, SHL, GAU, LSA and the BB INDEPTHII stations have similar broad-band responses to those of the instruments operated by us in northeast India. The SP INDEPTHII stations have short-period sensors.

To determine the Moho depth along the profile we use teleseismic receiver function analysis. The teleseismic *P*-wave coda contains *S* waves generated by *P* to *S* conversions at significant velocity discontinuities in the crust and upper mantle below the seismograph site. Receiver functions are radial and transverse waveforms created by deconvolving the vertical component waveforms from the radial and tangential component waveforms to isolate the receiver site effect from other information contained in the teleseismic *P*-wave coda (Langston 1979). Modelling the amplitude and timing of these conversions and their reverberations provides constraints on the underlying crustal structure. The use of receiver functions to determine crust and upper mantle velocity structure beneath three-component broad-band seismograph sites is now a well-established seismological technique. Various approaches for interpreting receiver functions have been discussed in the literature (Owens *et al.* 1984; Priestley *et al.* 1988; Kind *et al.* 1995; Sheehan *et al.* 1995; Zhu & Kanamori 2000). It is well known that receiver functions are primarily sensitive to high-wavenumber velocity changes and the velocity–depth product, not to velocity alone (Ammon *et al.* 1990). In this study we minimize the effect of the receiver function non-uniqueness by incorporating other geophysical constraints as *a priori* information in the interpretation of the receiver function observations.

We have computed teleseismic receiver functions for all magnitude 5.7 and greater events in the 30°–90° distance range using the iterative, time domain deconvolution technique of Ligorria & Ammon (1999). This method is based on a least-squares minimization of the difference between the observed horizontal seismogram and a predicted signal generated by the convolution of an iteratively updated spike train with the corresponding vertical component seismogram. To remove high-frequency noise, we applied a Gaussian low-pass filter with a corner at 0.7 Hz. Receiver functions for events lying in a limited backazimuth and epicentral distance ranges (Table 1) were averaged to improve the signal-to-noise ratio, and the ± 1 standard deviation (σ) bounds calculated. These bounds were used to constrain the inverted models and to evaluate how well particular phases of the waveform were identified.

To illustrate the details of the analysis procedure followed, we discuss the inversion of the BPN data. Fig. 2 shows the BPN receiver functions plotted as a function of back azimuth. In the 42°–155° backazimuth range, *Ps* is a clear arrival at 4 ± 0.5 s after *Pp*. This is followed by a clear positive arrival in some receiver functions at ∼14 s corresponding to the PpP_ms phase and a weak negative arrival at ∼17–19 s corresponding to the $PpS_ms + PsP_ms$. We average the three events in the Δ range 44°–48° and backazimuth 52°–72° (Table 1) to enhance the signal-to-noise ratio. The moveout over this 4° distance range is only 0.2 s, leading to a marginal broadening of the averaged *Ps* phase. The averaged receiver function shows prominent positive arrivals at ∼4 and ∼14 s and a weak negative arrival at ∼17–19 s. We identify these as the *Ps*, PpP_ms and $PpS_ms + PsP_ms$ arrivals, respectively. The *Ps* and PpP_ms arrivals are prominent phases in the three individual receiver functions (Fig. 3). The tangential receiver function has a weak arrival immediately following the direct *P* and no significant arrivals thereafter, indicating that the crustal structure beneath BPN is relatively homogeneous, in agreement with the small azimuthal variation in the timing of the *Ps* phase (Fig. 2).

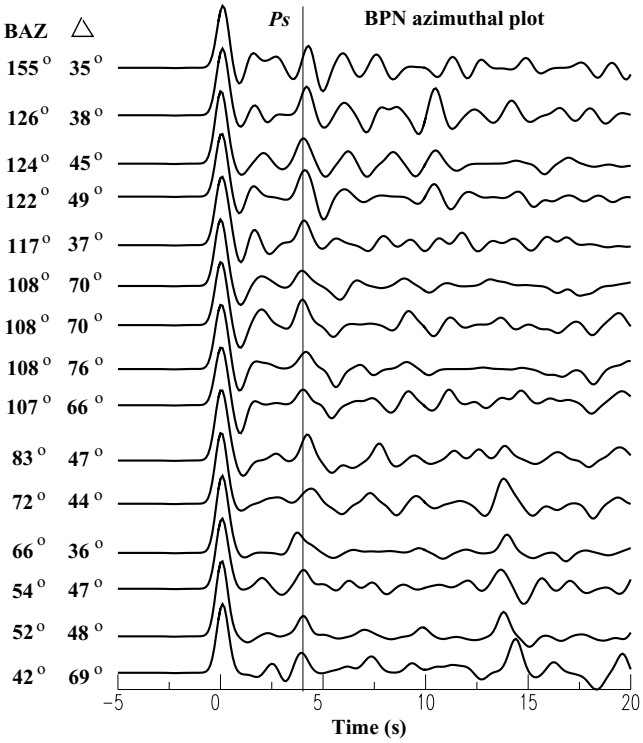

Figure 2. BPN radial receiver functions plotted as a function of backazimuth. The backazimuth (BAZ) and distance values (Δ) in degrees for each trace are given on the left. The average time of the *Ps* Moho conversion is denoted by the vertical line.

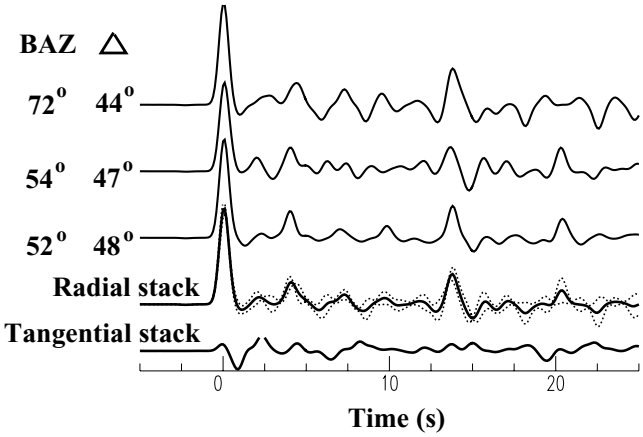

Figure 3. BPN receiver functions for a backazimuth bin of 52°–72° sampling the Shillong Plateau. The top three waveforms are individual radial receiver functions with the BAZ and Δ for each given on the left. The averaged radial receiver function with ±1 S.D. bounds is plotted beneath the individual radial receiver functions. The averaged tangential receiver function for the three events is shown at the bottom.

The thickness H and average V_p/V_s of the crust can be estimated from the relative timing of the conversions and reverberations (Zandt *et al.* 1995; Zhu & Kanamori 2000). The $Ps - Pp$ time difference is dependent on crustal thickness, average crustal velocity (either V_p or V_s) and the V_p/V_s ratio. The $PpP_ms - Ps$ time is the two-way P-wave traveltime, and the $(PpS_ms + PsP_ms) - Pp$ time is the two-way S-wave traveltime through the crust. The ratio of the $Ps - Pp$ and $PpP_ms - Ps$ times is independent of crustal thickness but weakly dependent on V_p. On the other hand, the ratio of the

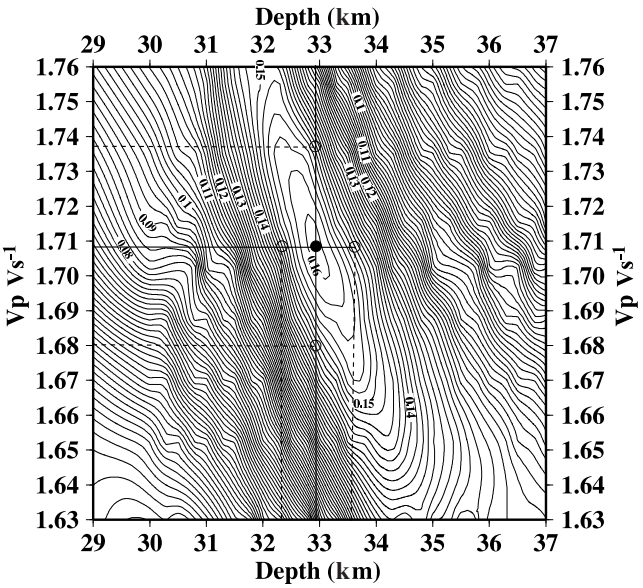

Figure 4. The V_p/V_s ratio versus crustal thickness for the average BPN receiver function shown in Fig. 3 calculated using the receiver function stacking technique of Zhu & Kanamori (2000). The crustal thickness beneath BPN is 1 ± 0.5 km and the average crustal V_p/V_s is 1.71 ± 0.03.

$PpP_ms - Ps$ and $(PpS_ms + PsP_ms) - Pp$ times is proportional to the V_p/V_s ratio and independent of crustal thickness (Zandt *et al.* 1995). We determine H and V_p/V_s using the stacking procedure of Zhu & Kanamori (2000) weighting the *Ps*, PpP_ms and $PpS_ms + PsP_ms$ phases as 0.7, 0.2 and 0.1, respectively and adopting reasonable values for the average P-wave velocity of the Shillong Plateau crust. For a reasonable range of crustal V_p (6.1–6.4 km s^{-1}) (De & Kayal 1990), we obtain a crustal thickness of 33 km and average V_p/V_s of 1.71 beneath BPN (Fig. 4). The estimated error in crustal thickness and V_p/V_s calculations over the range of V_p chosen is ∼2 km and ∼0.02, respectively. The ±1 S.D. bounds for the crustal thickness and V_p/V_s are 0.5 km and 0.03, respectively.

We determine the details of the crustal structure beneath BPN by inverting the averaged radial receiver function using the inversion algorithm of Herrmann (2003). The starting velocity model parametrized in terms of thin, homogeneous, horizontal layers of fixed equal thickness (2 km) was constructed from earlier published work (De & Kayal 1990; Singh 1994; Mukhopadhyay *et al.* 1997; Rai *et al.* 1999). The S-wave velocity is the free parameter in the inversion, the P-wave velocity is set by Poisson's ratio calculated from the V_p/V_s ratio for BPN and the density from the P-wave speed. Synthetic receiver functions were calculated for the mean ray parameter of the three events forming the average receiver function. The finely parametrized model was first inverted to determine the depth to the Moho and identify mid-crustal interfaces, if any. We then simplified the crustal model by grouping adjacent model layers with similar wave speeds to form a more coarsely parametrized velocity model and reinverted the receiver function. This procedure was repeated until we found the velocity model with the minimum number of parameters which fit the main features of the BPN receiver function (Figs 5a and c).

We then used forward modelling (Fig. 5b) to estimate how well the main features of the crustal model were constrained by arrivals in the observed receiver function. For example, we vary the Moho depth (Fig. 5d) from its inverted value and compare the synthetic receiver functions computed for the perturbed model with the

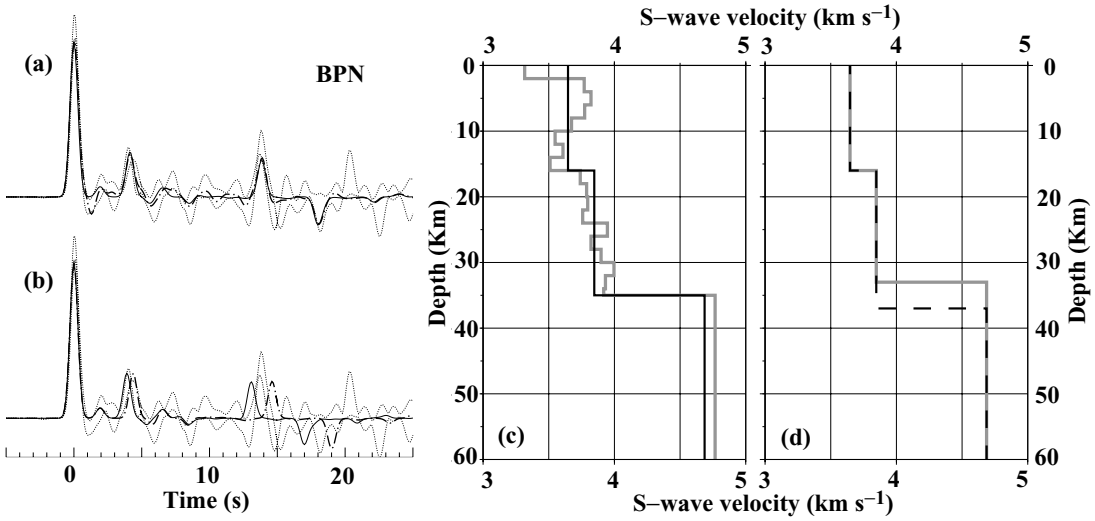

Figure 5. Inversion results for the BPN receiver function. The match of the ±1 S.D. bounds of the observed (dotted lines) and synthetic receiver function (bold line) shown on the left (a, b) calculated for the velocity model shown on the right (c, d). (a) Inversion results for the thin layer parametrization (grey line) and simplified model (black line) plotted in (c). (b) Test to determine bounds on the inverted Moho depth (±2 km) plotted in models (d). The timing of the *Ps* and PpP_ms phases strongly constrains the depth to the Moho.

observed receiver function to determine bounds on the Moho depth. The final velocity model thus obtained beneath BPN shows a two-layered crust, consisting of a 16 km thick ($V_s \sim 3.65$ km s^{-1}) upper layer and a 19 km thick ($V_s \sim 3.85$ km s^{-1}) lower layer, the Moho discontinuity lying at a depth of 35 ± 2 km (Table 1).

All other station data were analysed in the same manner as BPN and we present the final results of our analysis in Section 3 below.

3 CRUSTAL STRUCTURE AND MOHO GEOMETRY OF NORTHEAST INDIA

To compare various features of the crust as the Indian Plate penetrates Tibet, we plot individual and summed radial receiver functions for each station as depicted in Fig. 6. Although the northeastern Indian stations and the southeastern Tibetan stations do not lie on a linear profile across the Himalaya, the observed uniformity of the Himalaya along strike make this comparison of the two profiles meaningful. The receiver function traces are individually corrected for distance moveout of the Moho *Ps* phase to a reference distance of 67° and plotted northward from Karimganj. The average of the summed receiver functions is plotted in the left panel (Figs 6a and c); the individual receiver functions ordered first according to station location and second according to backazimuth are plotted equispaced in the right panel (Figs 6b and d). As pointed out by Yuan *et al.* (1997), the form of the plots in Figs 6(a) and (c) has the advantage of a constant distance scale but the disadvantage of making lateral correlation between traces more difficult, especially when there are gaps in the profile. The form of the plots in Figs 6(b) and (d) has the advantage of making phase correlation clearer but the disadvantage of a varying distance scale.

The northeastern Indian receiver functions, except for those from KMG and for southern and southeastern events recorded at CHP, are relatively simple and broadly similar to those observed on the south Indian Shield (Rai *et al.* 2003). The dominant feature of the northeastern Indian receiver functions is the Moho *Ps* phase whose delay time with respect to the direct *P* arrival increases from ∼4 s for the Shillong Plateau stations SHL, BPN and CHP (for northern arrivals), to ∼5 s for the Brahmaputra Valley sites BAI, GAU and TEZ and ∼6 s at the Lesser Himalaya site BMD, indicating a progressive deepening of the Moho northwards. The CHP receiver functions for southern backazimuths which largely sample the Bengal Basin are more complicated in that the direct *P* phase is followed by a strong negative arrival at ∼1 s delay, and later by strong positive arrivals at ∼3 and ∼8 s delay, and a weaker positive arrival at ∼5 s delay. We identify the 5 s arrival as the Moho *Ps* phase. If the 3 s arrival were the Moho *Ps* phase the crust would be abnormally thin beneath the Bengal Basin; if at 8 s, it would be abnormally thick. Neither is consistent with the meagre gravity data for the region (Verma & Mukhopadhyay 1977; Gaur & Bhattacharji 1983; Das Gupta & Biswas 2000). This is discussed further in the next section. The KMG receiver function has a ∼0.5 s delayed first arrival, followed by a large-amplitude positive arrival at ∼1.5 s and a negative arrival at ∼2.5 s. These features all result from the thick, low-velocity sediments below KMG.

Receiver functions at the Himalayan station of BMD show two equally strong positive arrivals at 3.5–4 s and at 6 s. We do not believe the earlier phase to be the Moho *Ps* because this would imply an extremely thin crust beneath the Lesser Himalaya which is inconsistent with gravity observations (Das Gupta & Biswas 2000). BMD lies between the mapped surface manifestations of the MCT and the MBT and the 3.5–4 s phase could result from conversion at the décollement surface along which the Indian Plate underthrusts Tibet, its upper part being scraped off and stacked to form the Himalaya. Splays from this décollement form the MCT, the MBT and another imbricate thrust called the Main Frontal Thrust (MFT) which has been mapped in the central Himalaya, extending the thrust front southward. The MBT has been geologically well demarcated in the eastern Himalaya and is clearly seen at the surface about 10 km north of the foothills. We therefore interpret the later arrival in the BMD receiver function to be the Moho *Ps* phase.

Figs 6(c) and (d) are essentially the same as Fig. 3 of Yuan *et al.* (1997), except that we have computed the receiver functions using a different method from Yuan *et al.* (1997) so we can present a consistent receiver function profile across the region. In comparison with those of northeastern India, the southeastern Tibetan receiver

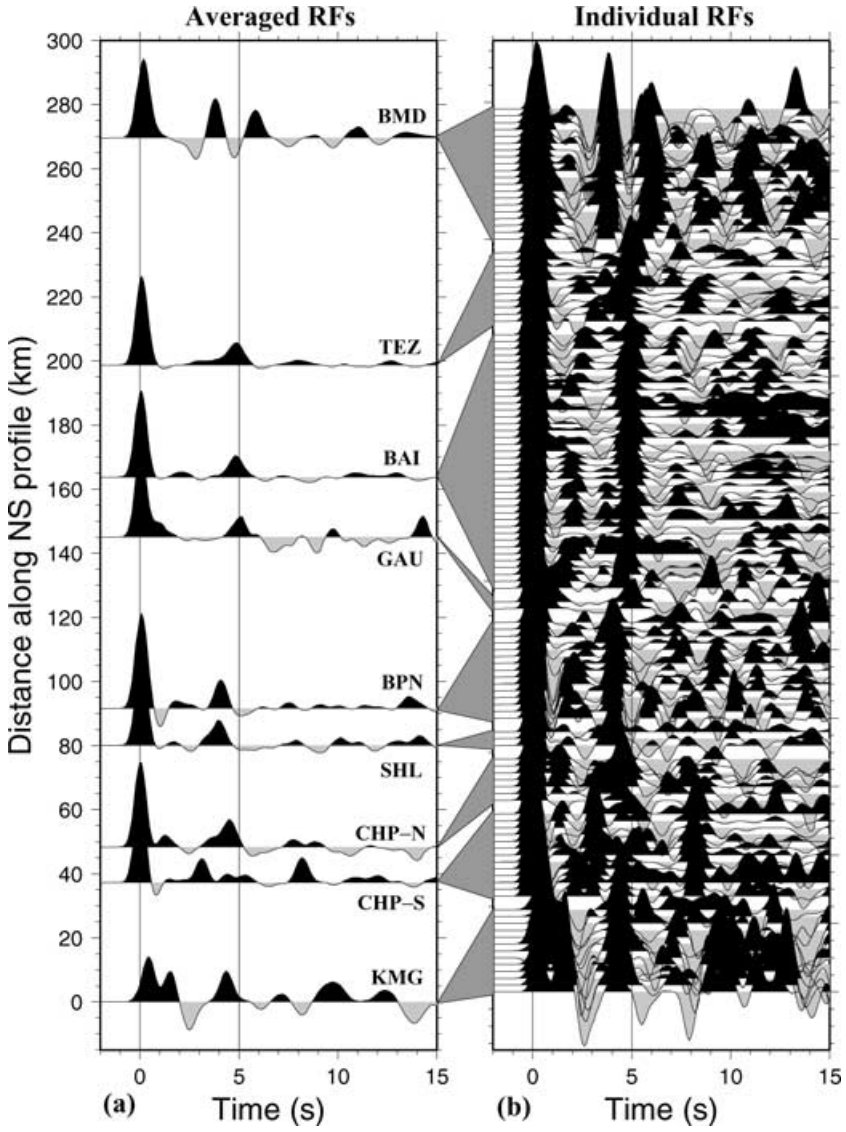

Figure 6. Plot of all receiver functions from the northeast Indian and INDEPTHII stations. (a) Averaged radial receiver functions plotted on a relative distance scale along the north–south profile from northeast India. (b) Plot of individual traces which were summed to form the average receiver functions in (a). (c) Averaged and (d) individual receiver functions from the INDEPTHII stations and LSA on the Tibetan Plateau. The individual traces are moveout corrected to a distance of 67° and have been plotted equally spaced from south to north sorted first by station and then by backazimuth. CHP is shown twice: CHP-N for events from the northeast and CHP-S for events from the southeast. BMD is shown at the top of (a) and (b) and repeated at the bottom of (c) and (d) for continuity. The average receiver functions shown in (a) and (c) are formed from all individual receiver functions from each station shown in (b) and (d), while averaged receiver functions formed from a few of these individual traces, over narrow distance range bins, have been used in the inversion for crustal structure.

functions are complex, implying that the crustal structure beneath southeast Tibet is much more complicated than the crustal structure beneath northeast India. The plot of these receiver functions, when viewed together with that for BMD, however, strongly suggests that it is the ∼7.5 s positive phase in the SP27 receiver function which corresponds to the Moho rather than the ∼11.5 s phase as interpreted by Yuan *et al.* (1997). Our interpretation would place the Moho at 62 km beneath SP27 and result in a fairly continuous deepening of the Moho from the Brahmaputra Valley (∼42 km) to southern Tibet (∼88 km), consistent with the gravity anomaly over the region.

3.1 Shillong Plateau

CHP is located at the southern end of the Shillong Plateau, just a few kilometres north of the Dauki Fault that separates the plateau from the Bangladesh plains. Here the fault is exposed as a pronounced scarp with more than 1 km vertical relief. Teleseismic arrivals from the north and northeast recorded at CHP sample the Shillong Plateau, whereas those from the south and southeast sample the downfaulted Bengal Basin (Fig. 1). Receiver functions from the two azimuths are very different in character. Those from events to the northeast (BAZ 52°–86°) show the *Ps* phase arriving at ∼4.5 s after the direct *P* wave (Fig. 7a), similar to the *Ps* − *Pp* time observed at BPN (Fig. 3), whereas those from the southeast (BAZ 106°–125°) show two prominent arrivals at ∼3 s and ∼8 s and a weak arrival at ∼5 s after the direct *P* wave (Fig. 7b). The inverted crustal model from the receiver functions from the northeastern events has an average V_s of 3.76 km s^{-1} and a Moho depth of 38 ± 2 km (Fig. 7e and Table 1). There are a number of possible interpretations for the ∼3, 5 and 8 s positive arrivals in the CHP-S receiver

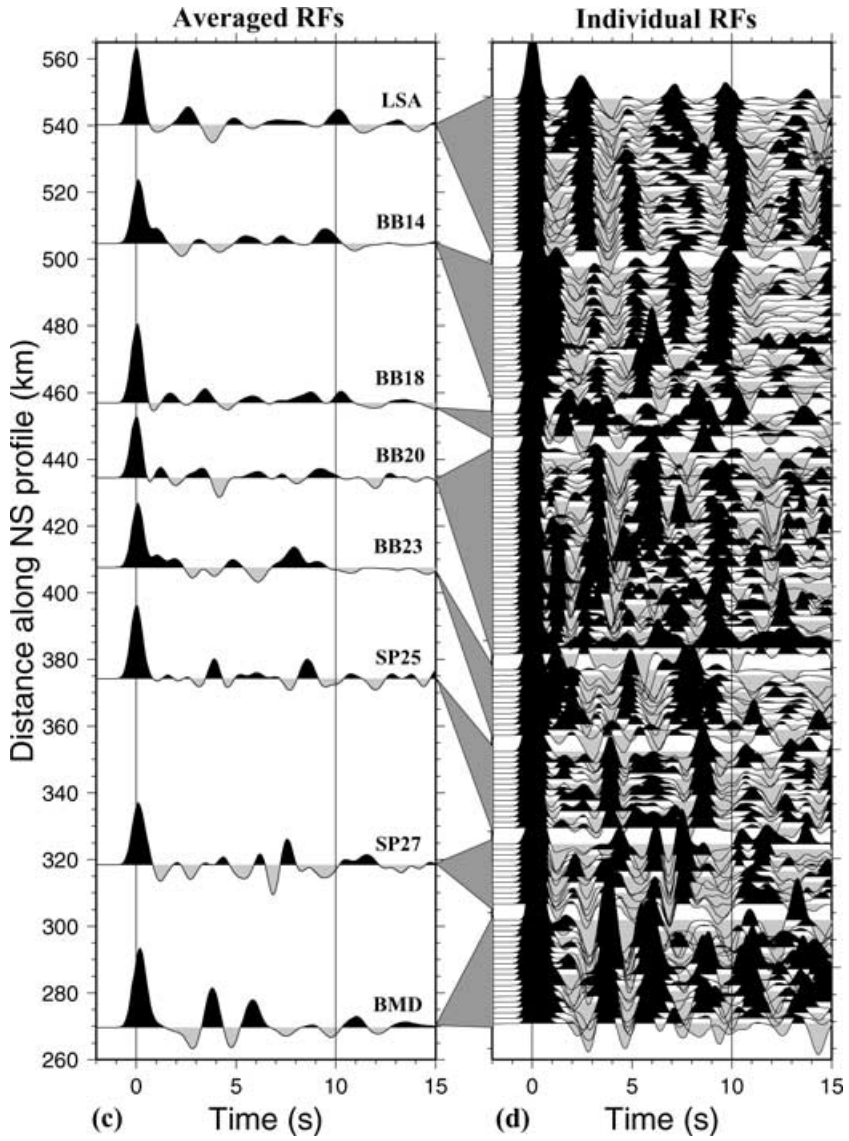

Figure 6.– (*Continued.*)

function. The character of the CHP-S receiver function could result from scattering which might deflect off-azimuth arrivals in the *P*-wave coda. To assess the strength of the off-azimuth arrivals we perform a polarization analysis on the CHP-S data and find the average deviation during the first 11 s of the *P* wave is ∼7.5° from the expected great circle azimuth. Therefore, although there is some indication of scattering in the *P*-wave arrival, we do not believe that this is the controlling factor in the CHP-S receiver function. The 3 s phase cannot be the Moho *Ps* as this would imply an abnormally thin (∼24 km) crust inconsistent with the known depth of sediments in the basin (Hiller 1988) and with the gravity data that are available for the region. Instead, it most likely represents the *Ps* phase conversion at the sediment–basement contact. The 8 s phase is also unlikely to be the Moho *Ps* phase as this would imply an abnormally thick (∼64 km) crust which is also inconsistent with known gravity anomalies along the Shillong–Bangladesh border. The 5 s phase is, therefore, the more likely Moho *Ps* phase as this implies the crust beneath the northern Bengal Basin to be 6–9 km thicker than beneath the southern Shillong Plateau, consistent with both the observed gravity (Verma & Mukhopadhyay 1977; Gaur & Bhattacharji 1983; Das Gupta & Biswas 2000) and topography. The larger amplitude of the 3 s and 8 s arrivals most likely arises from the substantial velocity contrast between the sediments and the basement compared with the velocity contrast across the Moho.

Inversion of the receiver function for events to the southeast of CHP indicates a crust with average V_s of 3.63 km s^{-1} and a Moho at 44 ± 2 km depth (Fig. 7f and Table 1). The model for the crust to the southeast of CHP contains a significant low-velocity layer between a depth of about 6 and 17 km. This is indicated by the significant negative arrival in the CHP-S receiver function immediately following the direct *P* arrival. Although CHP is located on the crystalline rocks at the southern edge of the Shillong Plateau, the final part of the ray paths for teleseismic events from the southeast sample the Bengal Basin crust. Wide-angle refraction studies in the Bengal Basin southwest of CHP show the existence of sediments ∼12 km thick overlying a basement dipping to the east (Kaila *et al.* 1992) while seismic soundings in Bangladesh (Hiller 1988) identified the top of the Eocene Sylhet limestone at a depth of 15 km in the Sylhet Trough south of the Dauki Fault. Furthermore, Sarkar *et al.* (1995) show that there is a high, positive velocity gradient in the sediments. The velocity in the low-wave-speed layer of the receiver function crustal model is consistent with the V_p velocity of

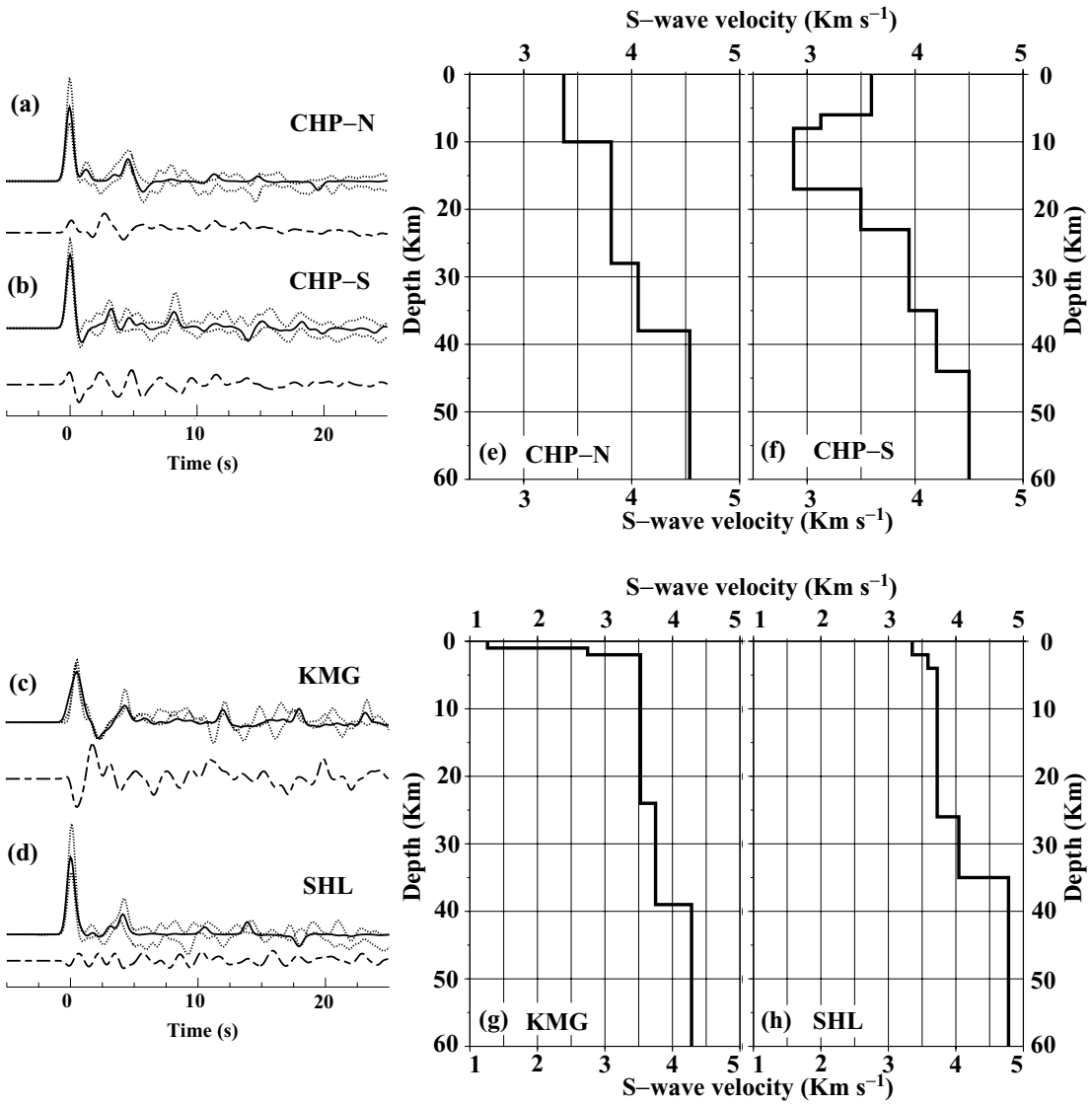

Figure 7. Inversion results for CHP, KMG and SHL receiver functions. CHP data are separated into north (a) and south (b) azimuths to illustrate the variation in crustal structure for rays sampling the Shillong Plateau and Bengal Basin. The match of the ±1 S.D. bounds of the observed (dotted lines) and synthetic receiver function (bold line) shown on the left (a–d) is calculated for the velocity model shown on the right (e–h). The average tangential receiver function for each site is shown below the radial receiver function.

the Bengal Basin sediments assuming a V_p/V_s of 1.73. Beneath the low-velocity layer at a depth of 17 km the crustal structure from the southeastern azimuth data shows a ∼6 km thick transitional zone qualitatively similar to the Shillong Plateau crust, underlain by a ∼12 km thick intermediate layer followed by a rather high-speed (V_s = 4.2 km s^{-1}) lower crust of ∼9 km thickness overlying the Moho (Fig. 7f).

The few seismograms with high signal-to-noise ratio, recorded at KMG in the Bengal Basin 60 km south of CHP, are for events to the northeast (BAZ 38°–42°, Table 1). The first arrival of the KMG receiver function is delayed and broadened and is followed by a significant negative arrival (Fig. 7c). Detailed analysis of the KMG receiver function incorporating what is known of the sediment structure from seismic refraction (Hiller 1988) suggests that the negative arrival is not the result of a velocity reversal at depth but is the $PpS_ms + PsP_ms$ arrival from the basement. Inversion of the averaged KMG receiver function (Fig. 7g) yields a Moho depth of 39 ± 2 km (Table 1) similar to that obtained from CHP-N which is understandable since the corresponding wave arrivals intersect the Moho near the southeastern edge of Shillong Plateau. For SHL ∼13 km south of BPN (Fig. 1) we had only three high signal-to-noise ratio seismograms from a distance range of 51°–65° and backazimuth 86°–109° (Table 1). From these seismograms we form the SHL average receiver function shown in Fig. 7d. The radial receiver function contains a prominent *Ps* arrival at ∼4 s following the direct *P* wave, similar to that seen at BPN, but the crustal reverberations are weak and the tangential receiver function shows a modest level of energy throughout the waveform. The inversion model (Fig. 7h) has an average crustal V_s of 3.77 km s^{-1} and a Moho at 35±2 km depth (Table 1), very close to those for BPN, but in addition shows a high-velocity layer in the lower crust.

3.2 Brahmaputra Valley

The stations GAU, BAI and TEZ are located on the foreland spur exposed in the Brahmaputra Valley. The average BAI receiver

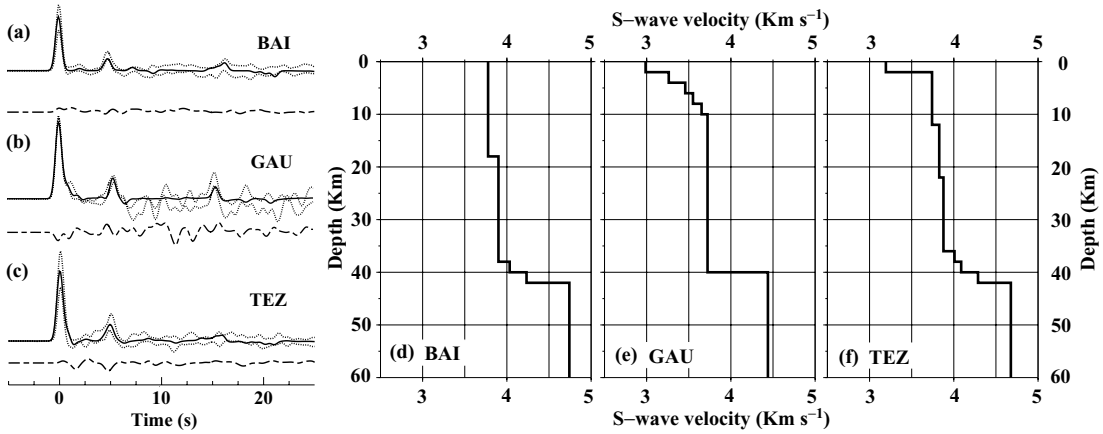

Figure 8. Inversion results for BAI, GAU and TEZ receiver functions. The figure format is the same as for Fig. 7.

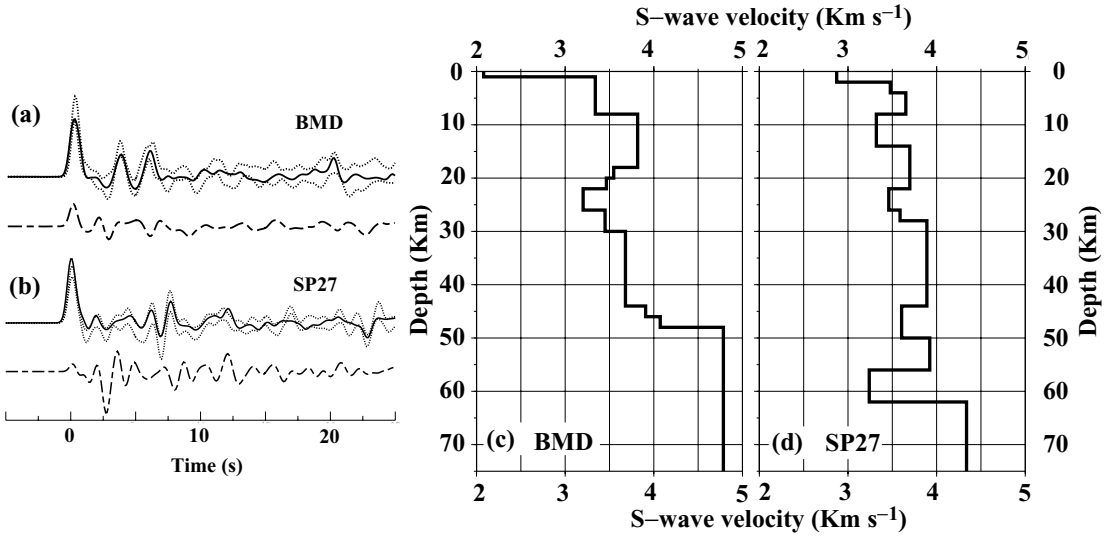

Figure 9. Inversion results for BMD and SP27 receiver functions. The figure format is the same as for Fig. 7.

function (BAZ 107°–117° and Δ67°–76°, Table 1), shows a prominent *Ps* arrival at ∼5 s following the direct *P* wave and a second, less prominent, positive arrival at ∼17 s which is consistent with the PpP_ms crustal reverberation (Fig. 8a). Using the stacking procedure of Zhu & Kanamori (2000), the crustal thickness and V_p/V_s ratio beneath BAI are found to be 41 ± 1 km and 1.73 ± 0.3, respectively. Inversion of the BAI radial receiver function gives a 42 ± 2 km thick crust consisting of an 18 km thick upper crust with $V_s = 3.77$ km s^{-1} underlain by a 24 km thick lower layer with $V_s = 3.93$ km s^{-1} (Fig. 8d and Table 1).

We have limited data from GAU and TEZ. Receiver function averages for GAU, formed from just two events, and TEZ, from seven, both show a prominent *Ps* phase at ∼5 s and significant arrivals at the expected time of the crustal reverberations (15–19 s) (Figs 8b and c). Inversion of the TEZ and GAU receiver functions yields crustal models (Figs 8e and f) similar to that found beneath BAI and adds confidence to the latter determination.

3.3 The Himalaya

Two stations sample the crust beneath the Himalaya (Fig. 1): BMD in the Lesser Himalaya of northeast India and the INDEPTHII station SP27 on the north side of the Great Himalayas in southern Tibet. The BMD receiver function (Fig. 9a) formed from an average of 10 seismograms (BAZ 90°–119° and Δ51°–61°, Table 1), shows two prominent positive peaks at ∼3.5 and ∼6.0 s (Fig. 9a) after the direct *P* arrival, with complex phases appearing in the earlier interval. The double peaks consistently appear in the individual BMD receiver functions (Fig. 6b). The tangential receiver function shows a significant arrival close to the direct *P* and additional arrivals in the first few seconds. As discussed earlier, we do not believe the 3.5 s positive phase in the BMD receiver function to be the Moho *Ps* phase, as this would imply a very thin crust (∼30 km) beneath the Lesser Himalayas (average elevation 2.8 km). The second positive phase at ∼6 s is more consistent with the anticipated crustal thickness for the Lesser Himalaya. Inversion of the BMD radial receiver function yields an average crustal V_s of 3.58 km s^{-1} and a Moho depth of 48 ± 2 km (Table 1). The phase arriving 3.5 s after *P* may result from the complex layering of the nappes and thrust sheets of the Lesser Himalaya formed from the stack of slivers scraped off from the Indian crust, and the pronounced velocity increase at 26–30 km depth in the BMD model may represent their base, along which the Indian Plate currently underthrusts the Himalaya and Tibet. However, since the MBT intersects the surface ∼30 km south of BMD, this seems

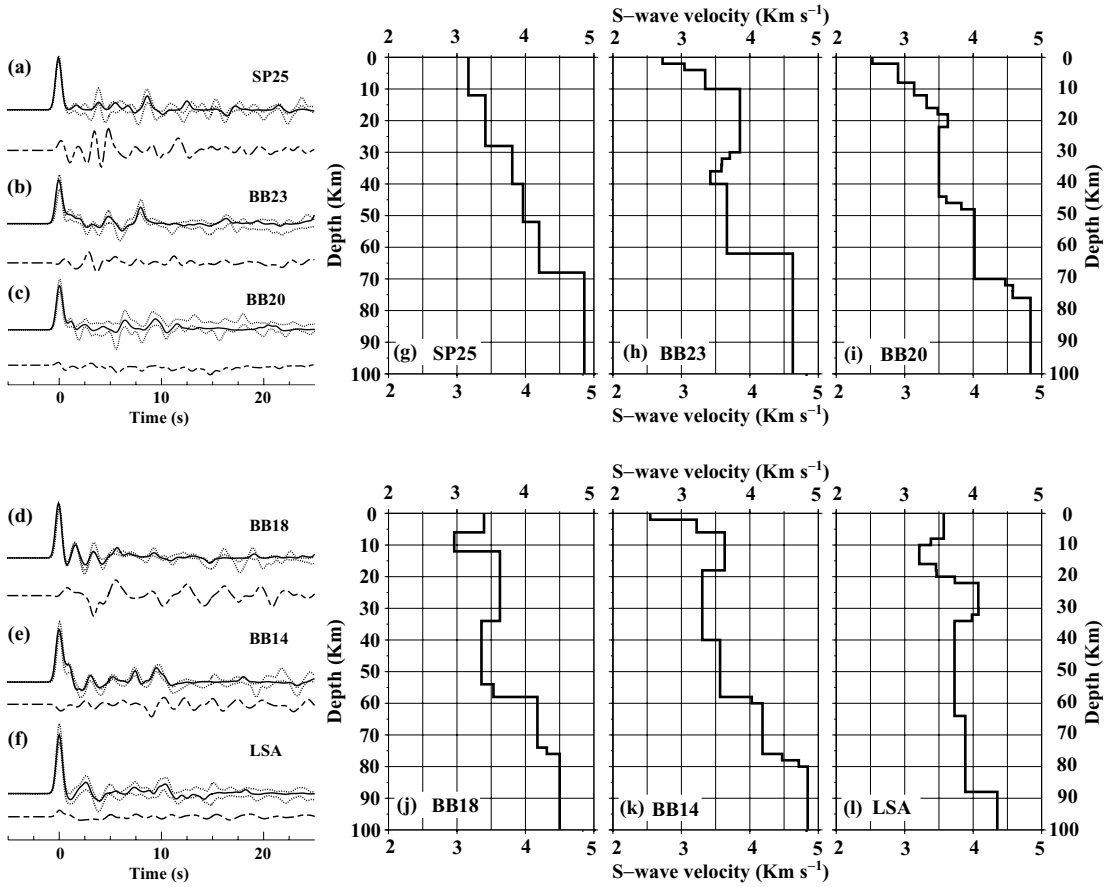

Figure 10. Inversion results for the INDEPTHII station (SP25, BB23, BB20, BB18 and BB14) and LSA receiver functions. The figure format is the same as for Fig. 7.

unusually deep for the décollement surface beneath BMD. The discontinuity at 8 km depth most likely corresponds to the décollement surface. The 3.5 s and 6.0 s phases do not constitute a double Moho in this region, as proposed by Hirn & Sapin (1984) further east in the Himalaya, since there is no suggestion of upper-mantle-like wave speeds immediately below the 26–30 km deep discontinuity. It is not yet clear what the structure between 26 and 30 km beneath BMD represents.

The receiver functions computed from the short-period INDEPTHII station SP27 are of lower quality than those determined from broad-band seismograms. However, the average receiver function for SP27 (Fig. 9b) consisting of 12 events (BAZ 50°–55° and Δ48°–54°, Table 1) shows prominent arrivals between ∼6.0 and 8.0 s. As explained in Section 3, we believe the positive arrival at 7.5 s to be the *Ps* conversion from the Moho. Yuan *et al.* (1997) interpreted this phase as a mid-crustal conversion and the lower-amplitude positive arrival at ∼11.5 s as the Moho *Ps* phase. The tangential receiver function shows moderate energy until ∼12 s following the *P* arrival, with a large arrival at 4–5 s. Inversion of the SP27 receiver function yields a complex crustal structure—presumably resulting from 3-D effects which are likely to be more severe in the short-period data—but the Moho is clear at a depth of 62 ± 2 km (Fig. 9d). The overlying crust has an average crustal V_s of 3.62 km s^{-1} (Table 1). The complexities within the crust from inversion of the SP27 receiver function are unlikely to be significant.

3.4 Tibetan Plateau

Teleseismic data were used to calculate receiver functions from four BB stations and one SP INDEPTHII station and the CDSN station LSA to determine the geometry of the Moho beneath the southern Tibetan Plateau (Fig. 1) and relate it to the northeastern Indian crust underthrusting southern Tibet. Kind *et al.* (1996) and Yuan *et al.* (1997), who previously inverted these data, used spatially filtered, smoothed receiver functions obtained by averaging each individual station receiver function with its neighbours to the north and south, before inverting for the crustal structure. This method improves the coherence between stations for the inversion of receiver functions, but in the presence of heterogeneity at discontinuities can lead to blurring of the feature on the averaged receiver function. This may be the reason for the Moho conversion being unclear in their spatially filtered receiver functions for stations 50 km north of the Zangbo Suture (Yuan *et al.* 1997). Therefore, rather than spatially filtering the receiver function, we simply averaged the individual radial receiver functions for a limited distance and backazimuth range of events (Figs 10a–f and Table 1) and analysed the average receiver function for each site separately in the same way as we did for the northeastern Indian sites.

We interpret and compare our inversion results with those of Kind *et al.* (1996) and Yuan *et al.* (1997) starting from station SP25 to LSA in the north. The most striking difference between our results

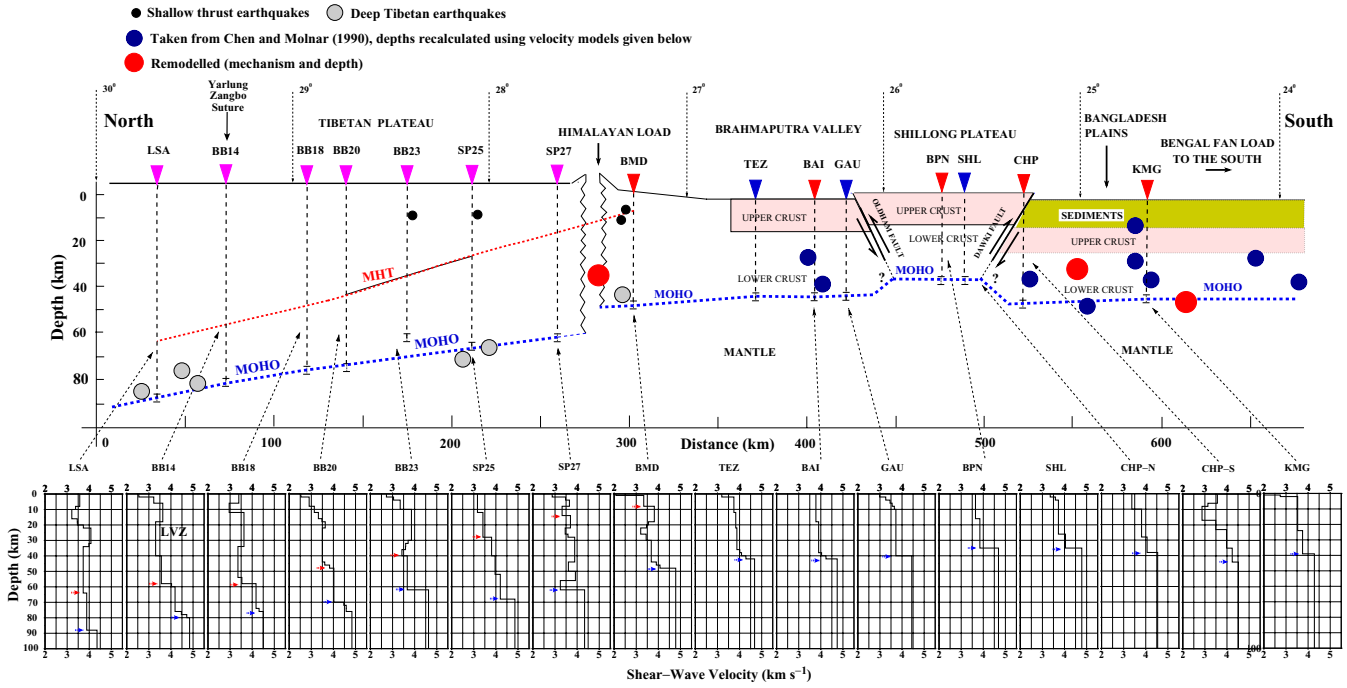

Figure 11. The upper part of the figure shows a schematic north–south profile from the southern Tibetan Plateau to the Bengal Basin; the lower part of the figure displays the receiver function crustal models at the 15 sites (two crustal models for CHP). The seismograph sites where we have determined the crustal structure using receiver function analysis are marked with inverted triangles in the upper part and the depth to the Moho denoted by vertical dashed lines with error bars beneath each seismic station. The Moho discontinuity and the Main Himalayan Thrust (MHT) are labelled (MOHO and MHT) and marked by a dashed line in the upper part and by arrowheads in the crustal velocity models below. Earthquakes ±350 km either side of the profile are projected onto the crustal cross-section in the upper part of the figure. The source of the hypocentral parameters for the earthquakes is indicated on the upper left. The relationship of the faults bounding the Shillong Plateau is taken from Bilham & England (2001).

and those of Yuan *et al.* (1997) is for the southernmost sites (SP25, BB23) where we determine the Moho to be 6–10 km shallower. The average receiver function from SP25 (A25 in Fig. 4 of Yuan *et al.* 1997) shows a double-peaked arrival at ∼7.5–8.0 s (1 s ahead of the other stations) following the direct *P*, which Yuan *et al.* (1997) interpreted as a merging of the conversions from the lower crustal discontinuity and the Moho, and yet determined the Moho to be at a similar depth as the other stations (A25 in Fig. 7 of Yuan *et al.* 1997). This could either be due to a faster model for the crust beneath SP25 (which is not the case as seen in Fig. 7 of Yuan *et al.* 1997) or a result of averaging the SP27, SP25 and BB23 receiver functions to form the A25 spatially filtered receiver function.

Our averaged SP25 receiver function (BAZ 50°–55° and Δ47°–53°, Table 1) has a strong arrival at ∼8.5–9.0 s (Figs 6d and 10a), which we interpret to be the Moho *Ps* phase. Inversion of the SP25 receiver function gives an average crustal V_s of 3.72 km s^{-1} and a Moho depth of 68 ± 2 km (Fig. 10g and Table 1), 6 km shallower than that inferred by Yuan *et al.* (1997). Their average receiver function for BB23 (A23 in Fig. 4 of Yuan *et al.* 1997) shows a very weak arrival at ∼9.5 s which they interpret as the *Ps* conversion from the Moho, but this feature is absent in their individual station receiver function average (Fig. 3 of Yuan *et al.* 1997). Our averaged BB23 receiver function (BAZ 44°–55° and Δ47°–54°, Table) shows a clear, large-amplitude arrival at 7.5–8.0 s (Figs 6d and 10b), which we interpret to be the Moho *Ps* phase. Inversion of the BB23 receiver function gives an average crustal V_s of 3.63 km s^{-1} and a Moho depth of 1 ± 2 km (Fig. 10h and Table 1), ∼10 km shallower than that found by Yuan *et al.* (1997). Our Moho depth of 76 km beneath BB20 is, however, (Figs 10c and i and Table 1) similar to the Yuan *et al.* (1997) model. Both the BB23 and the BB20 inversion models show a significant mid-crustal discontinuity between 40 and 50 km depth.

The main crustal feature north of the Zangbo Suture inferred by Yuan *et al.* (1997) was a pronounced low-velocity zone in the upper crust between a depth of 15 and 20 km. This has also been noted in the CMP profile (Nelson *et al.* 1996) at a depth of 15–18 km. In our inversion of data from BB14 we obtain a low-velocity zone (LVZ) at 18 km depth. Yuan *et al.* (1997) also found a shallower LVZ beneath LSA, and our inversion for the station closely matches their model. Our results show that a lower crustal discontinuity exists at a depth of 55–65 km beneath LSA and the northern INDEPTHII sites (BB18 and BB14, Fig. 1) and that the Moho deepens northwards from 76–88 km between these stations in agreement with the inversion of the spatially filtered receiver functions of Yuan *et al.* (1997). Results of our receiver function analysis are summarized in Fig. 11.

3.5 Intracrustal interface

The crustal models (Fig. 11) show a strong intracrustal interface deepening from a depth of ∼8 km beneath BMD to ∼65 km beneath LSA. This feature is best observed in the crustal models derived from broad-band data but is also evident in the model derived from short-period data. Nelson *et al.* (1996) identified a mid-crustal discontinuity in the INDEPTH CMP data recorded approximately between BB20 and SP25 (Fig. 11) and they determined this to be the Main Himalayan Thrust (MHT). They were unable to trace this feature further to the north because of the upper crustal bright spots which they interpreted as the presence of fluids in the crust and made imaging of deep crustal features impossible. The mid-crustal discontinuity between BB20 and SP25 in the CMP data coincides

with the intracrustal interface observed in the receiver function inversion models (Fig. 11). The receiver function analysis allows this discontinuity to be traced as shallow as a depth of ∼8 km beneath BMD, and as deep as ∼65 km beneath LSA (Fig. 11).

3.6 Moho geometry

Fig. 11 shows that the thinnest crust in northeast India (35–38 km) occurs beneath the Shillong Plateau. The plateau crustal structure (*Vs*, *H*) is similar to that observed beneath the Archean Eastern Dharwar Shield in south India (Rai *et al.* 2003). The thin crust and high elevation of the Shillong Plateau, where the Bouguer gravity anomaly has a small positive value of ∼20–40 mGal (Verma & Mukhopadhyay 1977; Gaur & Bhattacharji 1983; Das Gupta & Biswas 2000), support the model proposed by Bilham & England (2001) that the plateau is supported by slip on two reverse faults, the south-bounding Dauki and a north-bounding Oldham Fault, maintained by the prevailing compression of the Indian Plate. A comparison of the crustal velocity–depth sections (Figs 5, 7 and 8) under the Shillong Plateau and the Brahmaputra Valley sites show that although the latter has a 5–7 km deeper Moho, the lower crust beneath both areas is similar. The total crust beneath the Brahmaputra Valley no doubt represents the surviving Indian crust just after the Indo-Eurasian collision. What is found beneath the Shillong Plateau, on the other hand, is its somewhat eroded remnant which is thereby thinned.

Our analysis of the receiver functions for broad-band seismic data from southeast Tibet indicates the existence of a strong impedance interface at a depth of 68 km beneath SP25 deepening to 88 km beneath LSA. Earlier receiver function analysis (Yuan *et al.* 1997) and controlled-source seismic studies (Hauck *et al.* 1998) have suggested that this interface is the Moho. Our receiver function analysis also shows a progressive deepening of the Moho of the Indian Plate from ∼35 km under Shillong at an altitude of ∼1 km, to 40–42 km beneath the Brahmaputra Valley, 48 km beneath BMD at an altitude of ∼2.8 km in the Lesser Himalaya, and to 88 km under Lhasa at an altitude of 3.7 km in southern Tibet.

The crust of southern Tibet has been intensively studied using a variety of geophysical techniques, but little information is available for the crustal structure of northeast India. Crustal thickness beneath the Shillong Plateau estimated by Kayal & Zhao (1998), using body wave tomography, and by Gaur & Bhattacharji (1983), using gravity modelling, is qualitatively similar to our values of 35–38 km, as is the crustal structure proposed by Rai *et al.* (1999) from their seismic time-term study under the Brahmaputra Valley and the adjoining Lesser Himalaya.

The only other information on the crustal structure beneath the Himalaya exists for the central part of the range in Nepal. Early crustal models derived from modelling gravity data (Kono 1974) from this area showed that the Bouguer anomaly increased from −150 mGal at the MBT to −300 mGal beneath the Great Himalayas and −500 mGal beneath southern Tibet. This gravity variation was interpreted as indicating a moderately dipping Moho from the Himalayan foothills into Tibet, and the approximate doubling of crustal thickness from ∼35 km in northern India to ∼70 km in southern Tibet. Hirn & Sapin (1984), Hirn *et al.* (1984a,b) and Lepine *et al.* (1984) made the first sparse, controlled-source seismic measurements across southern Tibet, the Great Himalaya and the Lesser Himalaya. They found that the crust thickened from ∼55 km beneath the Great Himalayas to ∼75 km in southern Tibet, which is consistent with our receiver function results. However, the controlled-source seismic results from the central Himalaya indicated that the crustal thickening was not smooth and that the deepening of the Moho occurred step-wise. In addition, they found evidence for southward dips which locally brought the deeper northern segment of the Moho reflectors to underlie the shallower southern segment of the Moho. Our receiver function results are spatially too sparse to substantiate such Moho offsets, if they exist.

4 EARTHQUAKE FOCAL DEPTHS IN RELATION TO CRUSTAL THICKNESS

Studies of crustal structure and earthquake focal depths in northeast India have had a significant influence on ideas about the rheology of the continental crust. Most intraplate continental earthquakes occur in the upper ∼15 km of the crust, with rare earthquakes occurring at deeper levels in some areas. This observation of the depth distribution of intraplate continental earthquakes, coupled with laboratory measurements of rock properties as a function of temperature and pressure, led Chen & Molnar (1983) to propose that the continental crust consists of a brittle, seismically active upper layer and a weak, aseismic lower layer overlying a brittle uppermost mantle. For this rheology of the continental crust, the rock strength is primarily a function of temperature as has been observed in the oceanic crust (Chen & Molnar 1983; Wiens & Stein 1983). Typical continental thermal gradients lead to crustal rocks being brittle to depths of about 15 km and ductile at deeper levels, especially in the presence of small amounts of fluids. The change in mineralogy across the Moho puts the olivine-rich rocks of the uppermost mantle back into the strong, and perhaps brittle regime, provided they are dry (Mackwell *et al.* 1998).

One of the key observations supporting this view of continental crustal rheology was from northeast India and southeast Tibet (Chen & Molnar 1983, 1990) where calculated depths of earthquake foci were found to occur as deep as 52 km. Gravity modelling suggested that the crust of northeast India was 35–40 km thick, placing such earthquakes within the upper mantle. Both constraints on Moho depths and earthquake focal depths have improved significantly since 1990. Maggi *et al.* (2000a,b) examined more recent earthquakes in intraplate settings where upper mantle earthquakes were previously thought to occur and found that there was no evidence to support a bimodal depth distribution of earthquakes in these areas. Instead, they found a single seismogenic layer (T_s) whose thickness correlated well with the effective elastic thickness (T_e) for the continental crust (McKenzie & Fairhead 1997). However, they found that in continental areas like northern India, T_s extended down to ∼40 km, understandably deeper than T_e because the timescale of the seismic energy accumulation and release cycle was shorter than that involved in supporting uncompensated topography.

Accordingly, we re-examined earthquake focal depths in northeast India (Fig. 12). For moderate to larger events with sufficient data we determined their focal depths using waveform inversion of teleseismic *P* and *SH* waveforms (Appendix A). We also recomputed focal depths of the events in Chen & Molnar (1990), using our revised crustal structure for the region. These focal depths are superimposed on our crustal model for northeast India and southeast Tibet in Fig. 11. All events were found to occur within the crust or so close to the Moho that we cannot distinguish on which side of the Moho they might lie. However, since seismicity in the region suggests the lower crust to be seismically active, we suspect that the deepest earthquakes occur in the lowermost crust and not in the uppermost mantle.

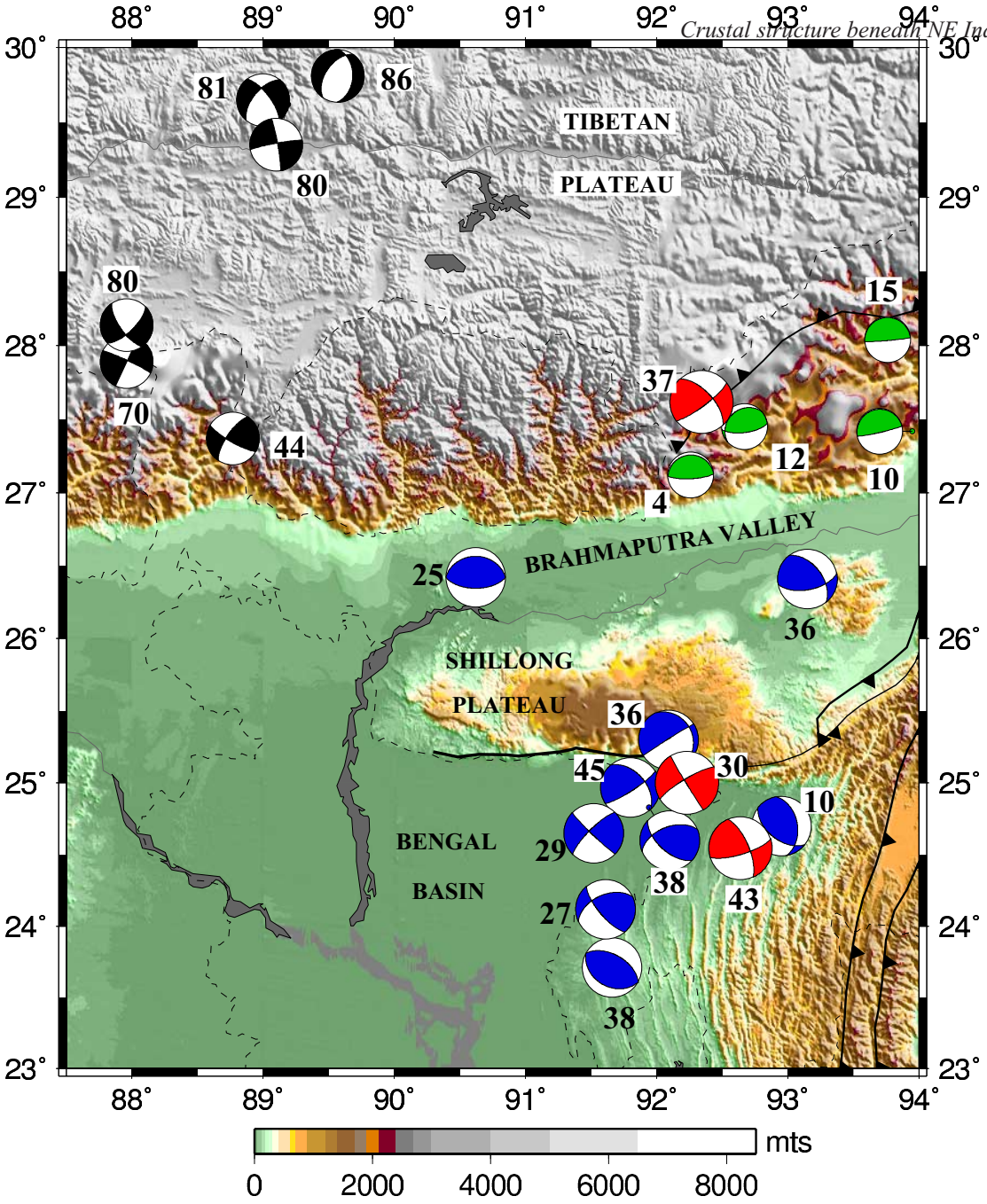

Figure 12. Focal mechanisms of earthquakes in northeast India and southern Tibet. Large black focal spheres represent the three earthquakes for which the source mechanisms and centroid depths are constrained by waveform modelling in this study (Figs A1, A3 and A5). The larger grey focal spheres are taken from Chen & Molnar (1990), with the depths (number beside the spheres) recalculated using the velocity models obtained from the receiver function inversion. Smaller dark grey focal spheres represent deep earthquakes in southern Tibet and shallow thrust events north of the Himalaya (see numbers beside spheres). Table A1 summarizes the references of the hypocentral parameters for the earthquakes.

Microearthquakes in northeast India, occurring as deep as 80 km below the surface, have been reported by Kayal *et al.* (1993), based on two microearthquake surveys in northeast India, one of which was centred ~25 km south of BMD. However, both networks consisted of only four stations and Kayal *et al.* (1993) analysed events with *S–P* times of 5 s or less. With the velocity structure from the receiver function analysis, a 5 s *S–P* interval places all of these events in the lower crust, which is consistent with results from more detailed microearthquake observations to the west in the Himalayas (Khattri *et al.* 1989; Pandey *et al.* 1995). Thus, there is no compelling evidence for either microearthquakes or moderate to large sub-Moho earthquakes occurring in the Shillong Plateau region. However, the fundamental issue is not whether the uppermost mantle beneath the region is seismically active or not but whether there exists a bimodal distribution of focal depths. The data we have for northeast India do not support the bimodal depth distribution for earthquakes.

5 SUMMARY AND CONCLUSIONS

We use broad-band teleseismic data recorded at eight sites along a north–south profile in northeast India to determine the seismic characteristics of the crust. The profile extends from Karimganj in the Bengal Basin, 50 km south of the eastern Shillong Plateau to

Bomdilla within a few kilometres of the MCT in the Himalaya. Receiver function analysis of these data show that the crust beneath the Shillong Plateau is 35–38 km thick and similar in character to the crust of the Archean shield in southern India (Rai *et al.* 2003). There is a ∼6 km offset in the Moho across the southern edge of the Shillong Plateau with the crust of the Bengal Basin being ∼44 km thick. Further to the north along the profile in the Brahmaputra Valley, the crust is 40–42 km thick and the Moho appears to dip gently to the north to a depth of ∼48 km beneath the Lesser Himalaya. The crystalline crust beneath the Bengal Basin, Shillong Plateau and Brahmaputra Valley appears to be similar in its lower parts, and the difference in the thicknesses arises primarily from the tectonic contexts: downfaulting and prolonged sedimentation in the Bengal Basin, erosion of the uplifted Shillong Plateau and flexure of the Himalayan foredeep north of the Brahmaputra Valley. The thin crust and high elevation of the Shillong Plateau support the pop-up structure for the plateau as proposed by Bilham & England (2001). We use data from six INDEPTHII (Yuan *et al.* 1997) seismographs and the CDSN station LSA to determine the crustal characteristics beneath the Great Himalaya and the southern Tibetan Plateau to the north of our northeast India profile. Beneath the Great Himalaya the Moho marking the base of the underthrusting Indian crust lies at a depth of ∼62 km, and progressively deepens under the southern Tibetan Plateau from ∼68 km, north of the Great Himalayas, to ∼88 km beneath LSA. The difference in the Himalayan and Tibetan crust results from stacking fractured slivers of the leading edge of the underthrusting Indian crust forming the Himalaya, and thickening the Tibetan crust above the Indian Plate.

We have re-examined earthquake focal depths in northeast India. For recent moderate-sized events we have determined the focal parameters using *P*- and *SH*-waveform inversion. For older moderate-sized events we use the results of Chen & Molnar (1990) with the focal depths adjusted for the velocity structure of our crustal model. We find all these events to occur within the crust or so close to the Moho that we cannot distinguish on which side of the Moho they lie. Thus, we find no evidence of significant seismicity occurring below the crust in this region nor evidence for a bimodal focal depth distribution.

From the foregoing analysis, we visualize a picture of the crust in northeast India, the eastern Himalaya and southern Tibet as shown in Fig. 13. While we are unable to fully resolve the details of the crust south of the Shillong Plateau apart from placing the Moho at a depth of ∼44 km, the plateau itself appears propped up against the steeply dipping Dauki Fault on its southern margin and the Oldham Fault on its northern margin (Bilham & England 2001). Mid to Upper Cretaceous marine fossils on the southern part of the plateau indicate a shelf environment (Das Gupta & Biswas 2000) during that time. However, from the Mid-Cretaceous the region experienced uplift with major uplift occurring in the Mid-Miocene, within the new compressional regime resulting from the continent–continent collision. The plateau now has an average elevation of ∼1 km and a small positive Bouguer gravity anomaly (Das Gupta & Biswas 2000) indicating that it does not have a mantle root.

The Shillong Plateau structure provides additional information on the relative strength of the lower crust and uppermost mantle. If we consider a weak lower crust over a strong mantle, the lower crust would be expected to flow, thereby increasing the crustal thickness beneath the plateau while maintaining a relatively flat Moho (McKenzie & Jackson 2002); this would result in a negative Bouguer gravity anomaly. Erosion would reduce the elevation of the plateau, but its crust would be slightly thicker than that of the surrounding region, given the present average elevation of ∼1 km. On the other hand, for a strong lower crust over a weaker upper mantle the void left by the plateau uplift would be replaced by mantle material resulting in an antiroot and a small positive Bouguer gravity anomaly, as observed in this case (Das Gupta & Biswas 2000). Erosion would leave the plateau with a slightly thinner crust, which is what our receiver function analysis reveals.

The crust of the Indian Shield is flexed downward north of the Brahmaputra Valley as it underthrusts the Himalaya and the southern Tibetan Plateau, its base highlighted by the large impedance contrast interface found from the receiver function analysis as well as controlled-source seismic experiments, and delimiting the deepest occurring earthquakes. The uppermost significant interface beneath BMD, although not as clearly demarcated in the inverted crustal model, probably marks the décollement surface along which the Indian Plate underthrusts southern Tibet and which is further highlighted by the loci of great earthquakes in the Himalaya (Seeber & Armbruster 1981). Earthquakes beneath northeast India are confined to a single seismogenic layer and we find no evidence for a double seismic zone with depth in the region.

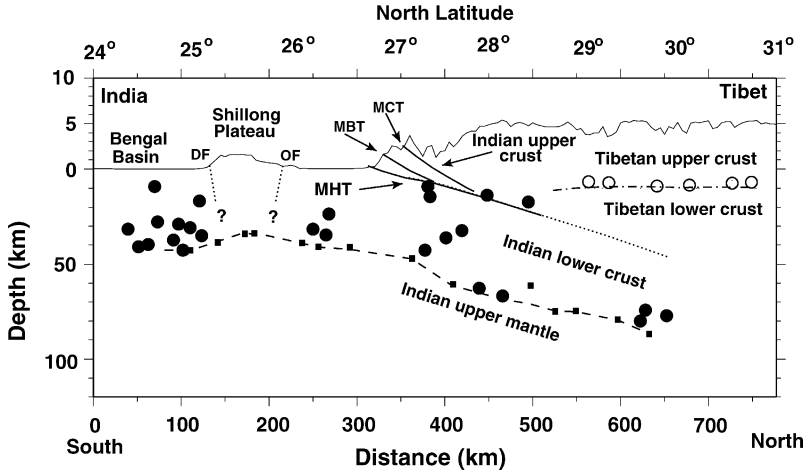

Figure 13. Schematic cross-section through the northeast India–southeast Tibet collision zone at approximately 91.7°E. A different vertical exaggeration is used above and below sea level. The squares denote the receiver function Moho depth estimates. Earthquakes shown in Fig. 12 are projected onto the profile plotted as black circles. The Shillong Plateau is bounded by the Dauki Fault (DF) and the Oldham Fault (OF).

ACKNOWLEDGMENTS

We thank Dr S. K. Laskar, Dr Ashok Kumar and Mr Nava Kumar Hazarika of Tezpur University for support in maintaining the broad-band stations in northeastern India, and we are grateful to Dr Dulal Goswami, Gauhati University, the directors of IMD, New Delhi, and NGRI, Hyderabad for granting permission to use data from their respective broad-band stations at Gauhati, Tezpur and Shillong. Data from the INDEPTHII deployment and the LSA station were provided by the IRIS DMS. We thank James Jackson, Peter Molnar and Roger Bilham for providing insights during numerous discussions and for critically reading the manuscript. The constructive review of Anne Sheehan has helped greatly in improving the original version of the manuscript. Figs 1, 12, 13 and all velocity models were plotted using GMT.

REFERENCES

Ammon, C., Randall, G. & Zandt, G., 1990. On the nonuniqueness of receiver function inversions, *J. geophys. Res.,* **95,** 15 303–15 318.

Baranowski, J., Armbruster, J., Seeber, L. & Molnar, P., 1984. Focal depths and fault plane solutions of earthquakes and active tectonics of the Himalaya, *J. geophys. Res.,* **89,** 6918–6928.

Bilham, R. & England, P., 2001. Plateau pop-up in the 1897 Assam earthquake, *Nature,* **410,** 806–809.

Bilham, R. *et al.*, 1997. GPS measurements of present-day convergence across the Nepal Himalaya, *Nature,* **386**(6620), 61–64.

Chen, W.-P. & Molnar, P., 1977. Seismic moments of major earthquakes and the average rate of slip in Central Asia, *J. geophys. Res.,* **82,** 2945–2969.

Chen, W.-P. & Molnar, P., 1983. Focal depths of intracontinental and intraplate earthquakes and their implications for the thermal and mechanical properties of the lithosphere, *J. geophys. Res.,* **88,** 4183–4214.

Chen, W.-P. & Molnar, P., 1990. Source parameters of earthquakes and intraplate deformation beneath the Shillong Plateau and northern Indoburman ranges, *J. geophys. Res.,* **95,** 12 527–12 552.

Das Gupta, A. & Biswas, A., 2000. *Geology of Assam,* Geological Society of India, Bangalore.

De, R. & Kayal, J., 1990. Crustal *P*-wave velocity and velocity ratio study in northeast India by a microearthquake survey, *Pure appl. Geophys.,* **134**(1), 93–108.

Ekström, G., 1987. A broad band method of earthquake analysis, *PhD thesis,* Harvard University, Cambridge, MA.

Gansser, A., 1964. *Geology of the Himalayas,* InterScience, London.

Gaur, V. & Bhattacharji, J., 1983. *Gravimetric Determination of the Shape of Moho in Peninsular and NE India,* IUGG, XVIII General Assembly, Hamburg, Germany, 15–27 August 1983, 936p.

Hallet, B. & Molnar, P., 2001. Distorted drainage basins as markers of crustal strain east of Himalaya, *J. geophys. Res.,* **106**(B7), 13 697–13 709.

Hauck, M., Nelson, K., Brown, L., Zhao, W. & Ross, A., 1998. Crustal structure of the Himalayan orogen at similar to 90 degrees east longitude from Project INDEPTH deep reflection profiles, *Tectonics,* **17,** 481–500.

Herrmann, R.B., 2003. *Computer Programs in Seismology,* p. 110, St Louis University, MO, USA.

Hiller, K., 1988. *On the Petroleum Geology of Bangladesh,* Bundesanstalt fur Geowissenschaften und Rohstoffe und Geologische Landesamter in der Bundesrepublic Deutsch, Hannover.

Hirn, A. & Sapin, M., 1984. The Himalayan zone of crustal interaction : suggestions from explosion seismology, *Ann. Geophys.,* **2**(2), 123–130.

Hirn, A. *et al.*, 1984a. Crustal structure and variability of the Himalayan border of Tibet, *Nature,* **307**(5946), 23–25.

Hirn, A., Wittlinger, G., Zhong-Xin, X. & En-Yuan, G., 1984b. Main features of the upper lithosphere in the unit between the High Himalayas and the Yarlung Zangbo Jiang suture, *Ann. Geophys.,* **2**(2), 113–118.

Holt, W., 1989. The active tectonics and structure of the Eastern Himalayan Syntaxis and surrounding regions, *PhD thesis,*University of Arizona, Tucson, AZ.

Holt, W., Ni, J., Wallace, T. & Haines, J., 1991. The active tectonics of the eastern Himalayan syntaxis and surrounding regions, *J. geophys. Res.,* **96**, (B9),14 595–14 632.

Kaila, K., Reddy, P., Mall, D., Venkateswarul, N., Krishna, V. & Prasad, A., 1992. Crustal structure of the West Bengal basin, India from deep seismic-sounding investigations, *Geophys. J. Int.,* **111**, (1),45–66.

Kayal, J. & Zhao, D., 1998. Three-dimensional seismic structure beneath Shillong Plateau and Assam Valley, northeast India, *Bull. Seism. Soc. Am.,* **88,** 667–676.

Kayal, J., De, R. & Chakraborty, P., 1993. Microearthquakes at the Main Boundary Thrust in eastern Himalaya and the present-day tectonic model, *Tectonophysics,* **218**, (4),375–381.

Khattri, K., Chander, R., Gaur, V., Sarkar, I. & Kumar, S., 1989. New seismological results on the tectonics of the Garhwal Himalaya, *Earth planet. Sci. Lett.,* **98,** 91–109.

Kind, R., Kosarev, G. & Petersen, N., 1995. Receiver functions at the stations of the German Regional Seismic Network (GRSN), *Geophys. J. Int.,* **121,** 191–202.

Kind, T. *et al.*, 1996. Evidence from earthquake data for a partially molten crustal layer in Tibet, *Science,* **274,** 1692–1694.

Kono, M., 1974. Gravity anomalies in east Nepal and their implications to the crustal structure of the Himalayas, *Geophys. J. R. astr. Soc.,* **39,** 283–300.

Langston, C., 1979. Structure under Mt. Rainer, Washington, inferred from teleseismic body waves, *J. geophys. Res.,* **84,** 4749–4762.

Le Fort, P., 1975. Himalayas: the collided range, present knowledge of the continental arc, *Am. J. Sci.,* **275A,** 1–44.

Lepine, J., Hirn, A., Pandey, M. & Tater, J., 1984. Features of the *P*-waves propagated in the crust of the Himalayas, *Ann. Geophys.,* **2**(2),119–122.

Ligorria, J. & Ammon, C., 1999. Iterative deconvolution and receiver-function estimation, *Bull. Seism. Soc. Am.,* **89,** 1395–1400.

Mackwell, S., Zimmerman, M. & Kohlstedt, D., 1998. High-temperature deformation of dry diabase with application to tectonics on Venus, *J. geophys. Res.,* **103,** 975–985.

Maggi, A., Jackson, J., McKenzie, D. & Priestley, K., 2000a. Earthquake focal depths, effective elastic thickness, and the strength of the continental lithosphere, *Geology,* **28,** 495–498.

Maggi, A., Jackson, J., Priestley, K. & Baker, C., 2000b. A re-assessment of focal depth distribution in southern Iran, the Tien Shan and northern India: do earthquakes really occur in the continental mantle?, *Geophys. J. Int.,* **143,** 629–661.

McCaffrey, R. & Abers, J., 1988. *SYN3: a Program for Inversion of Teleseismic Body Wave Form on Microcomputers,*Technical Report AFGL-TR-0099, Air Force Geophysical Laboratory, Hanscomb Air Force Base, MA.

McCaffrey, R. & Nabelek, F., 1987. Earthquakes, gravity and the origin of the Bali Basin: an example of a nascent continental fold-and-thrust belt, *J. geophys. Res.,* **92,** 441–460.

McKenzie, D. & Fairhead, D., 1997. Estimates of the effective elastic thickness of the continental lithosphere from Bouguer and free air gravity anomalies, *J. geophys. Res.,* **102,** 27 523–27 552.

McKenzie, D. & Jackson, J., 2002. Conditions for flow in the continental crust, *Tectonics,* **21**(6), doi:10.1029/2002TC001394.

Molnar, P. & Chen, W.-P., 1983. Focal depths and fault plane solutions of earthquakes under the Tibetan Plateau, *J. geophys. Res.,* **88,** 1180–1196.

Molnar, P. & Lyon-Caen, H., 1989. Fault plane solutions of earthquakes and active tectonics of the Tibetan Plateau and its margins, *Geophys. J. Int.,* **99,** 123–153.

Molnar, P. & Pandey, M., 1989. Rupture zones of great earthquakes in the Himalayan region, *Proc. Indian Acad. Sci. (Earth Planet. Sci.),* **98,** 61–70.

Molnar, P., Chen, W.-P., Fitch, T. J., Tapponnier, P., Warsi, W. E. K. & Wu, F., 1977. Structure and tectonics of the Himalaya: a brief summary of relevant geophysical observations, in *Himalaya: Sciences de la Terre,* Colloque

Internationaux du CNRS no 268, pp. 269–294, Editions du Centre Nationale de la Recherche Scientifique, Paris.

Mukhopadhyay, S., Chander, R. & Khattri, K., 1997. Crustal properties in the epicentral tract of the great 1897 Assam earthquake, northeast India, *Tectonics,* **283,** 311–330.

Nabelek, J., 1984. Determination of earthquake source parameters from inversion of body waves, *PhD thesis,* Massachusetts Institute of Technology, Cambridge, MA.

Nandy, D. & Das Gupta, S., 1986. Application of remote sensing in regional geological studies - a case study in northeastern part of India, in *Proceedings of the International Seminar on Photogrammetry and Remote Sensing for Developing Countries,* pp. T.4–P./6.1–T.4–P/6.4. Survey of India, New Delhi, India.

Nelson, K. *et al.*, 1996. Partially molten middle crust beneath southern Tibet: synthesis of project INDEPTH results, *Science,* **274,** 1684–1688.

Ni, J. & Barazangi, M., 1984. Seismotectonics of the Himalayan collision zone—geometry of the underthrusting Indian plate, *J. geophys. Res.,* **89,** 1147–1163.

Owens, T.J., Zandt, G. & Taylor, S.R., 1984. Seismic evidence for an ancient rift beneath the Cumberland Plateau, Tennessee: a detailed analysis of broadband teleseismic *P*-waveforms, *J. geophys. Res.,* **89,** 7783–7795.

Pandey, M., Tandukar, R., Avouac, J., Lave, J. & Massot, J., 1995. Interseismic strain accumulation on the Himalayan crustal ramp (Nepal), *Geophys. Res. Lett.,* **22,** 751–754.

Priestley, K., Zandt, G. & Randal, G., 1988. Crustal structure in eastern Kazakh, U.S.S.R. from teleseismic receiver functions, *Geophys. Res. Lett.,* **15,** 613–616.

Priestley, K., Baker, C. & Jackson, J., 1994. Implications of earthquake focal mechanism data for the active tectonics of the south Caspian Basin and surrounding regions, *Geophys. J. Int.,* **118,** 111–141.

Rai, S., Prakasam, K. & Agrawal, N., 1999. *Pn* wave velocity and Moho geometry in northeastern India, *Proc. Indian Acad. Sci. (Earth Planet. Sci.),* **108**(4), 297–304.

Rai, S., Priestley, K., Suryaprakasam, K., Srinagesh, D., Gaur, V. & Du, Z., 2003. Crustal shear velocity structure of the south Indian shield, *J. geophys. Res.,* **108**(B2), doi:10.1029/2002JB001776.

Sarkar, D., Reddy, P., Kaila, K. & Prasad, A., 1995. Multiple diving waves and high-velocity gradients in the Bengal sedimentary basin, *Geophys. J. Int.,* **121**(3), 969–974.

Seeber, L. & Armbruster, J., 1981. Great detachment earthquakes along the Himalayan arc and long-term forecasts, in *Earthquake Prediction:*

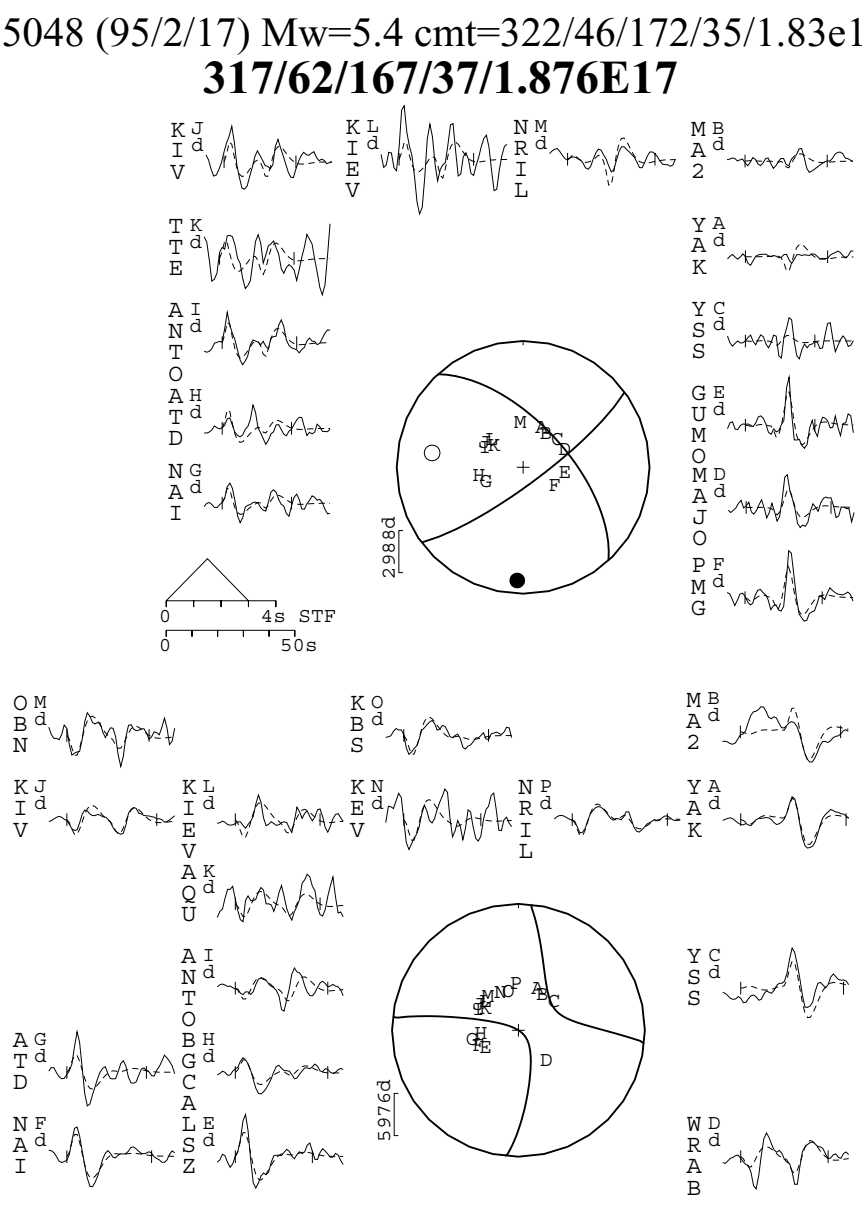

Figure A1. 1995 February 17 earthquake in the Himalayas. Minimum misfit solution: strike 317°, dip 62°, rake 167°, depth 37 km, M_w 5.4.

an International Review, Maurice Ewing Series **Vol. 4,** pp. 259–277, eds Simpson, D. & Richards, P., American Geophysical Union, Washington, DC.

Shamsuddin, A. & Abdullah, S., 1997. Geologic evolution of the Bengal Basin and its implication in hydrocarbon exploration in Bangladesh, *Indian J. Geol.,* **69,** 93–121.

Sheehan, A.F., Abers, G.A., Jones, C.H. & Lerner-Lam, A.L., 1995. Crustal thickness variation across the Colorado Rocky Mountains from teleseismic receiver functions, *J. geophys. Res.,* **100,** 20 391–20 404.

Singh, D., 1994. Shear wave velocity structure over the eastern Indian subcontinent, *Tectonophysics,* **230,** 127–134.

Verma, R.K. & Mukhopadhyay, M., 1977. An analysis of gravity field in northeastern India, *Tectonics,* **42,** 283–317.

Wiens, D. & Stein, S., 1983. Age dependence of intraplate seismicity and implications for lithospheric evolution, *J. geophys. Res.,* **88,** 6455–6468.

Yuan, X., Ni, J., Kind, R., Mechie, J. & Sandvol, E., 1997. Lithospheric and upper mantle structure of southern Tibet from a seismological passive source experiment, *J. geophys. Res.,* **102,** 27 491–27 500.

Zandt, G., Myers, S.C. & Wallace, T.C., 1995. Crust and mantle structure across the Basin and Range–Colorado Plateau boundary at 37°N latitude and implications for Cenozoic extensional mechanism, *J. geophys. Res.,* **100,** 10 529–10 548.

Zhu, L. & Helmberger, D., 1996. Intermediate depth earthquakes beneath the India–Tibet collision, *Geophys. Res. Lett.,* **23,** 435–438.

Zhu, L. & Kanamori, H., 2000. Moho depth variation in southern California from teleseismic receiver functions, *J. geophys. Res.,* **105,** 2969–2980.

APENDIX A: FULL-WAVEFORM INVERSION SOLUTIONS

The best-determined earthquake focal mechanisms and depths are those based on an analysis of teleseismic *P* and *SH* waveforms. This appendix contains the results of *P* and *SH* waveform modelling we have carried out for three recent earthquakes in the northeast Indian region. To model the waveforms of these earthquakes we took digital broad-band records from stations of the GDSN in the epicentral range 30–90° and convolved them with a filter that reproduces the bandwidth of the WWSSN 15–100 s long-period instruments. We then used the MT5 version of the McCaffrey & Abers (1988) algorithm which inverts the *P* and *SH* waveform data to obtain the strike, dip, rake, centroid depth, seismic moment and the source–time function, which is parametrized by a series of isosceles triangle elements of half-duration τ s. We constrained the source to be a double-couple. Our method and approach, and the way in which we estimated uncertainties in source parameters, are described in detail elsewhere (Nabelek 1984; McCaffrey & Nabelek 1987; Molnar & Lyon-Caen 1989; Priestley *et al.* 1994 e.g.). For these events, the centroid depth is well constrained to within ±5 km, the strike and rake to within ±10° and the dip to within 10°.

Figs A1, A3 & A5 show *P* (top) and *SH* (bottom) observed (solid) and synthetic (dashed) waveforms for the solutions in Table A1, which usually correspond to the final inversion result, or the 'minimum misfit' solution. Station positions on the *P* (top) and *SH* (bottom) focal spheres are identified by capital letters and arranged clockwise starting from the north. STF is the source–time function. Vertical ticks on the seismograms indicate the inversion window. Numbers beneath the header line are strike, dip, rake, centroid depth (km) and moment (N m). Stations were weighted according to azimuthal density and then the *S* seismogram weights were halved to compensate for their larger amplitudes. Comments appropriate to individual earthquakes are given in the figure captions.

Figs A2, A4 & A6 show several lines of observed (solid) and synthetic (dashed) seismograms at particular stations, each line corresponding to a solution whose strike/dip/rake/depth/M_0 is given in the header above the *P* (left) and *SH* (right) focal spheres on the left. The purpose of this type of figure is to demonstrate the sensitivity of the waveforms to a particular source parameter (usually depth) in cases where there were insufficient waveforms to carry out a full inversion for all source parameters of the sort displayed in Figs A1, A3 & A5. Explanations of each line of waveforms are given in the individual figure captions (A1–A6).

Table A1. Hypocentral and focal mechanism parameters with references for all earthquakes plotted in Fig. 12. The numbers in brackets in the depth column are the recalculated depths using our receiver function inversion models for events from Chen & Molnar (1990).

No.	Date (yr/mo/day)	Lat. (°N)	Long. (°E)	Depth (km)	Strike	Dip	Rake	Reference
1	1963/06/19	24.97	92.06	52(45)	57	80	42	Chen & Molnar (1990)
2	1963/06/21	25.13	92.09	38(36)	238	88	−70	Chen & Molnar (1990)
3	1964/10/21	28.04	93.76	15	265	3	90	Baronowski *et al.* (1984)
4	1964/09/01	27.12	92.26	4	267	13	90	Holt (1989)
5	1966/09/26	27.49	92.61	12	228	25	58	Holt (1989)
6	1968/06/12	24.83	91.94	41(38)	132	60	135	Chen & Molnar (1990)
7	1968/04/18	26.42	90.62	29(25)	90	60	90	Chen & Molnar (1990)
8	1968/12/27	24.12	91.61	29(27)	140	72	138	Chen & Molnar (1990)
9	1970/02/19	27.42	93.95	10	257	5	90	Molnar *et al.* (1977)
10	1971/06/02	23.71	91.66	46(38)	119	36	90	Chen & Molnar (1990)
11	1971/07/17	26.41	93.15	36(36)	79	60	46	Chen & Molnar (1990)
12	1973/08/01	29.59	89.17	81	220	60	−24	Molnar & Chen (1983)
13	1976/09/14	29.81	89.57	86	215	52	−68	Chen & Molnar (1977)
14	1980/11/19	27.37	88.77	44	214	71	12	Ekström (1987)
15	1984/12/30	24.64	92.89	10(10)	350	45	122	Chen & Molnar (1990)
16	1988/02/06	24.65	91.52	31(29)	225	77	5	Chen & Molnar (1990)
17	1991/12/21	27.90	88.14	70	295	85	180	Zhu & Helmberger (1996)
18	1992/03/07	29.62	89.19	80	350	85	−175	Zhu & Helmberger (1996)
19	1992/04/04	28.15	87.98	80	046	68	−23	Zhu & Helmberger (1996)
20	1995/02/17	27.61	92.34	37	317	62	167	This study
21	1996/11/19	24.54	92.63	43	73	74	22	This study
22	1997/05/08	25.00	92.23	30	239	79	2	This study

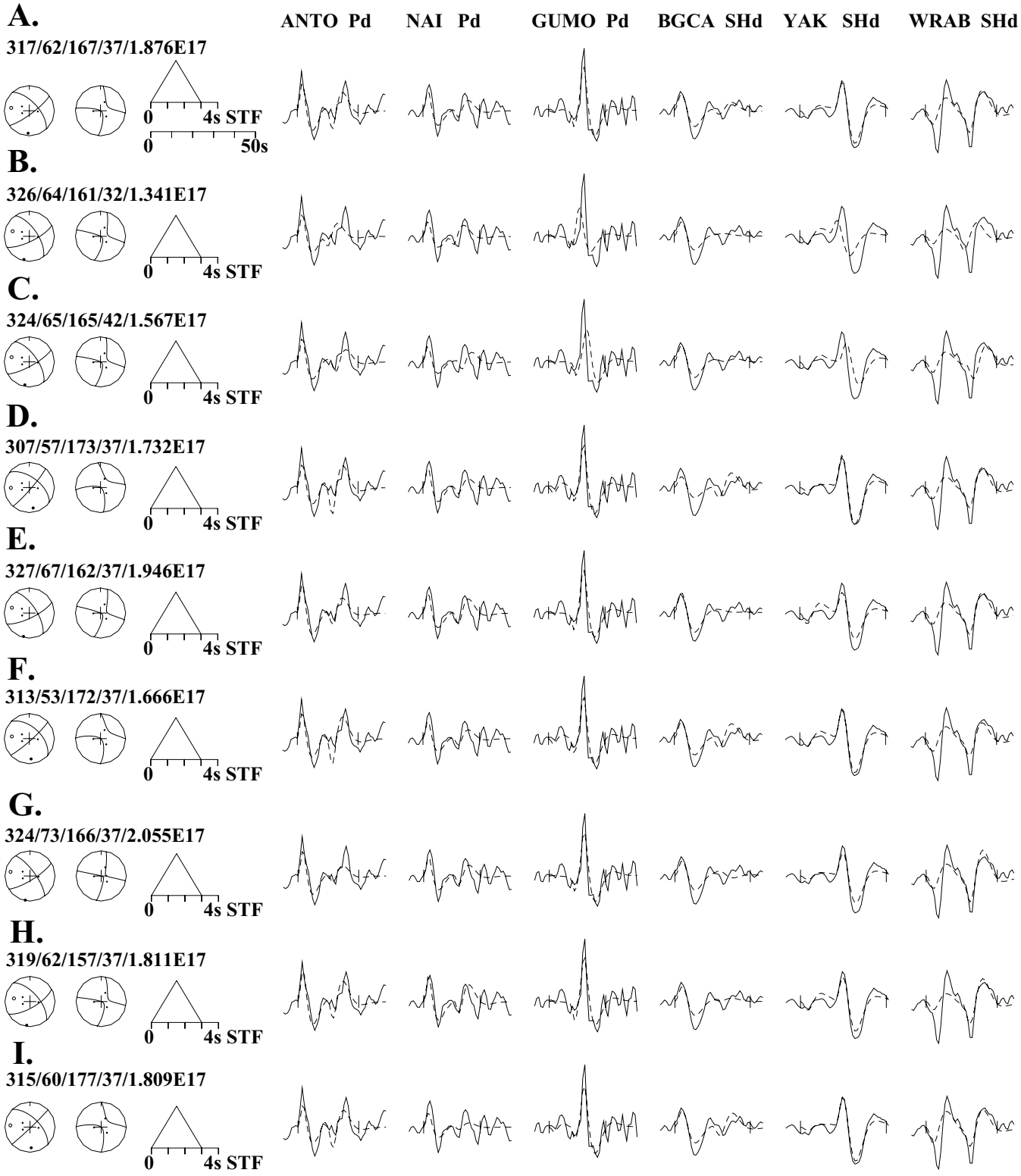

Figure A2. Sensitivity analysis for the earthquake in Fig. A1 done with three seismograms each for the *P* and *SH* waveforms. A: Minimum misfit solution. B and C: Depth fixed at 32 km and 42 km (37 ± 5 km) respectively; depth phases change in amplitude and moveout. D and E: Strike fixed at 307° and 327° (317 ± 10°) respectively; dip and rake of the nodal planes change to fit the data. First arrival amplitude matches deteriorate. F and G: Dip fixed at 53° and 73° (62 ± 10°) respectively; strike and rake of the nodal planes change to fit the data. H and I: Rake fixed at 157° and 177° (167 ± 10°) respectively; strike and dip of the nodal planes change to fit the data.

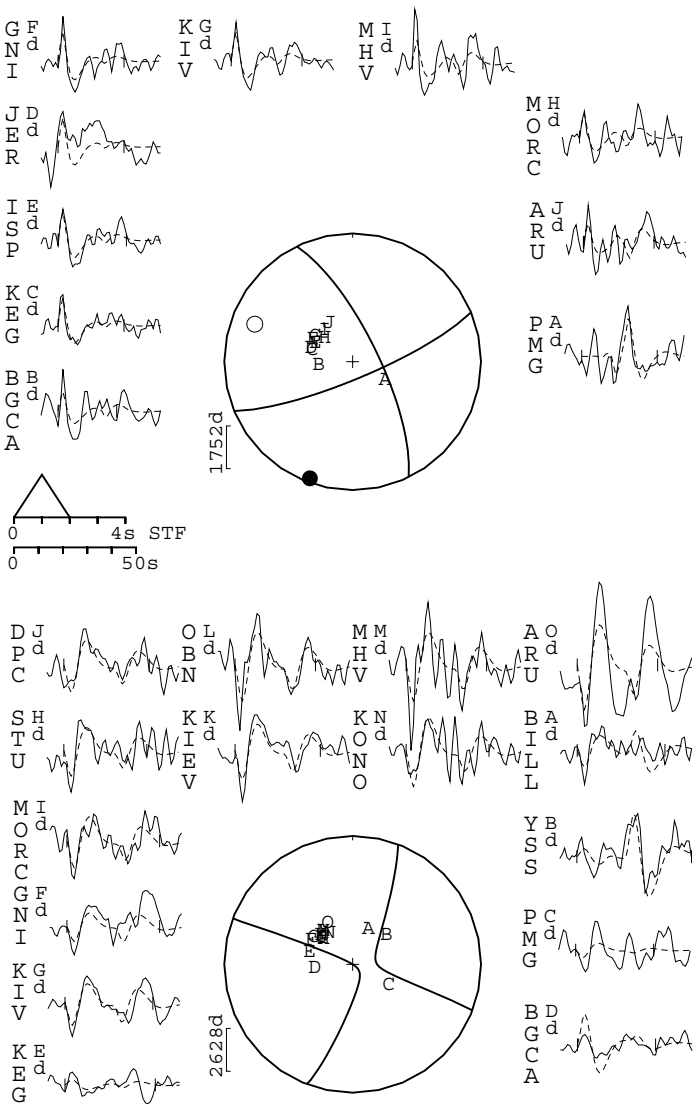

Figure A3. 1996 November 19 earthquake in the Bangladesh plains. Minimum misfit solution: strike 67°, dip 79°, rake 17°, depth 43 km, M_w 5.3.

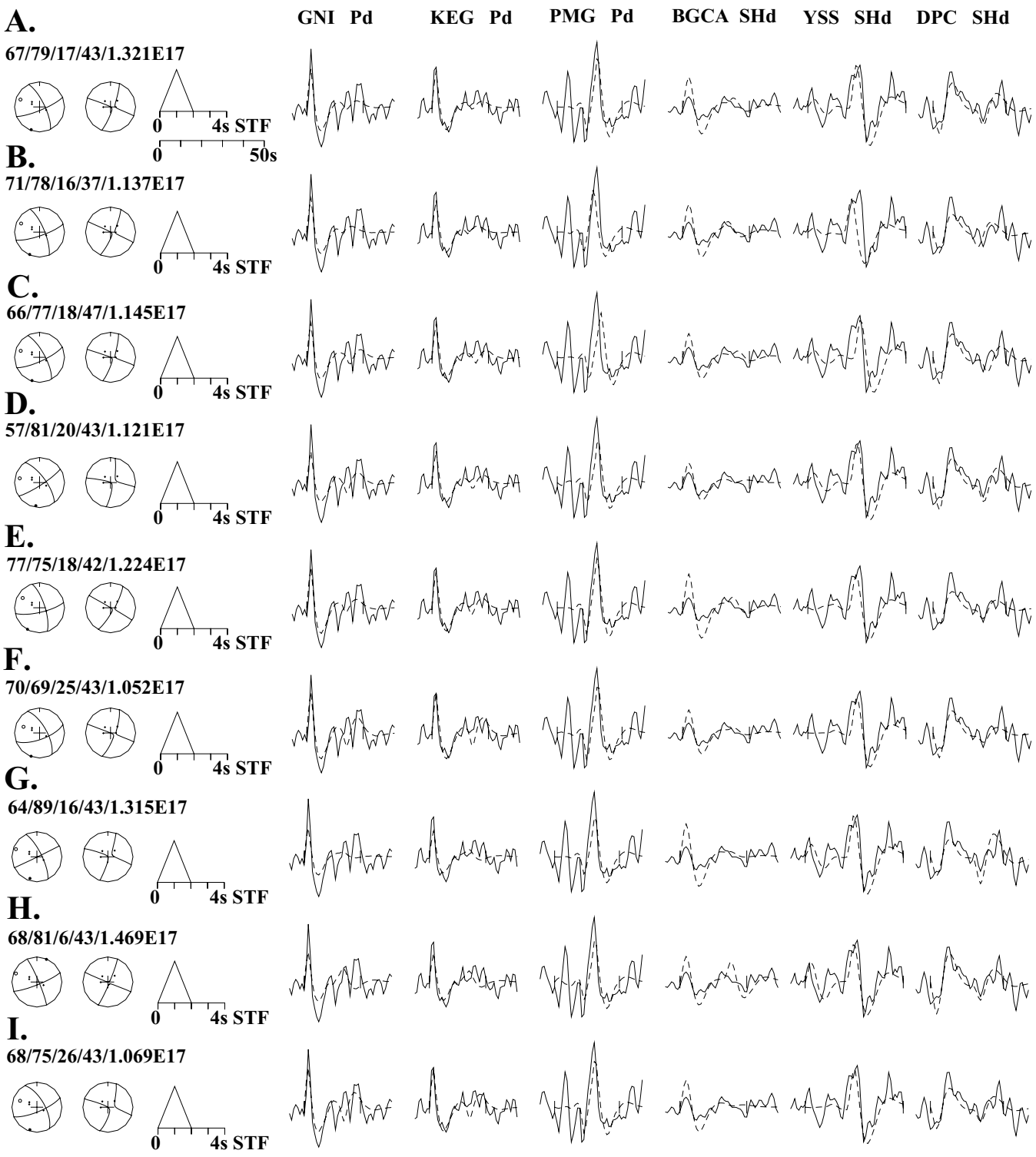

Figure A4. Sensitivity analysis for the earthquake in Fig. A3 done with three seismograms each for the *P* and *SH* waveforms. A: Minimum misfit solution. B and C: Depth fixed at 37 km and 47 km respectively; depth phases change in amplitude and moveout. D and E: Strike fixed at 57° and 77° (67 ± 10°) respectively; dip and rake of the nodal planes change to fit the data. F and G: Dip fixed at 69° and 89° (79 ± 10°) respectively; strike and rake of the nodal planes change to fit the data. H and I: Rake fixed at 6° and 267° (167 ± 10°) respectively; strike and dip of the nodal planes change to fit the data.

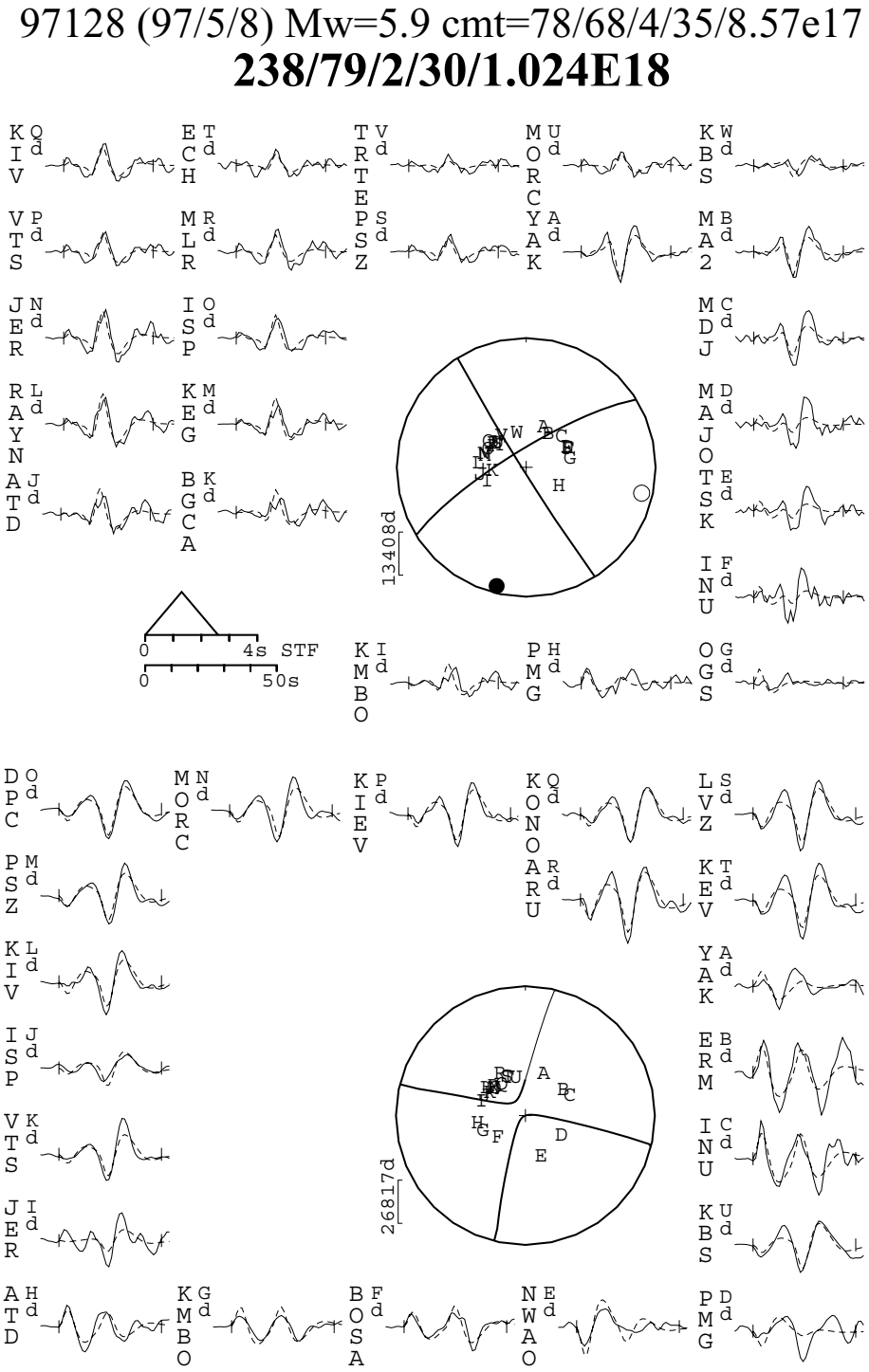

Figure A5. 1997 May 8 earthquake in the Bangladesh plains. Minimum misfit solution: strike 238°, dip 79°, rake 2°, depth 30 km, M_w 5.9.

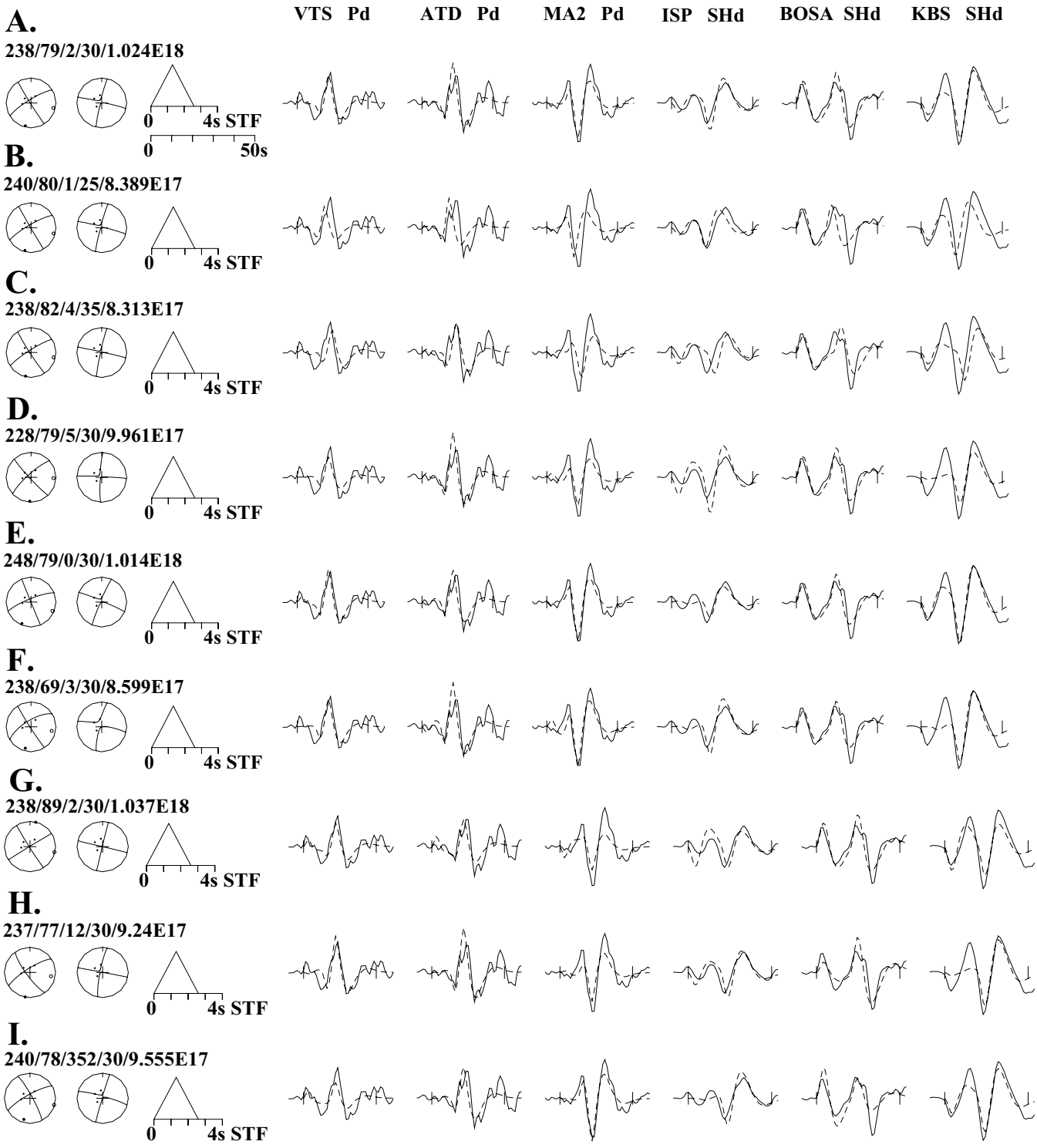

Figure A6. Sensitivity analysis for the earthquake in Fig. A5 done with three seismograms each for the *P* and *SH* waveforms. A: Minimum misfit solution. B and C: Depth fixed at 25 km and 35 km respectively; depth phases change in amplitude and moveout. D and E: Strike fixed at 228° and 248° (238 ± 10°) respectively; dip and rake of the nodal planes change to fit the data. F and G: Dip fixed at 69° and 89° (79 ± 10°) respectively; strike and rake of the nodal planes change to fit the data. H and I: Rake fixed at 12° and 352° (2 ± 10°) respectively; strike and dip of the nodal planes change to fit the data.